

===== TRANSLATIONS OF PUBLISHED ARTICLES =====

# **Determination of the Structure of Biological Macromolecular Particles Using X-Ray Lasers. Achievements and Prospects**

**Petrova T.E., Lunin V.Y.**

*Institute of Mathematical Problems of Biology RAS, Keldysh Institute of Applied Mathematics of Russian Academy of Sciences, Pushchino, Russia*

**Annotation.** X-ray diffraction analysis is the main experimental approach to the determination of the atomic structure of biological macromolecules and their complexes. The most serious limitation of its applicability, which is caused by the extremely low intensity of the rays scattered by a single molecule, today, is the necessity to prepare a sample of the object under study in the form of a single crystal. The commissioning of X-ray free-electron lasers with their super-powerful (by many orders of magnitude exceeding the brightness of modern synchrotrons) and ultra-short (less than 100 fs) pulses is an experimental breakthrough, which allows us to expect to obtain diffraction patterns from individual biological particles and determine their structure. The first experimental results demonstrate the proof-of-principle of the approach and are accompanied by the publication of a large number of articles devoted to various aspects of the development of the method. The purpose of this review is to describe the current state of art in this area, evaluate the results achieved, and discuss the prospects for further development of the method based on the analysis of articles in the world scientific literature published in recent years and the experience of the authors and their colleagues.

**Key words:** *biological macromolecules, single particles, X-ray scattering, X-ray free electron lasers, phase problem, biological crystallography.*

## **1. X-RAY DIFFRACTION EXPERIMENT**

### **1.1. Organization of a standard diffraction experiment in biological crystallography**

An X-ray diffraction experiment (X-ray diffraction analysis) is the main source of the information about the structure of biological macromolecules at atomic resolution. A standard scheme of the X-ray diffraction experiment is as follows (Figs. 1, 2). The object under study is fixed on a special device (goniometric head), which allows controlled rotation of the object. The object is irradiated by a monochromatic X-ray beam (primary beam). The result of irradiation is the appearance of new (secondary) X-rays (also called reflections), which propagate from the object in all directions. A part of these secondary rays hit a two-dimensional matrix of detectors located behind the object. In the literature, the word "detector" usually refers to the entire physical device, i.e., the entire matrix and related electronics. We use the word "matrix" to emphasize that this device consists of a huge number, up to several million independent elements that detect radiation in particular directions. Each of these elements measures the intensity of the beam that hits it, or more precisely, the energy that came to it during the exposure of the object. The total set of intensities recorded by the matrix of detectors is called an X-ray frame, or "image", which

recalls the early years of biological crystallography when a cassette with a photographic film served as a detector matrix. The complete experiment consists in collecting a set of X-ray images corresponding to different orientations of the object relative to the primary beam, which is achieved by rotating the object between the exposures of individual frames.

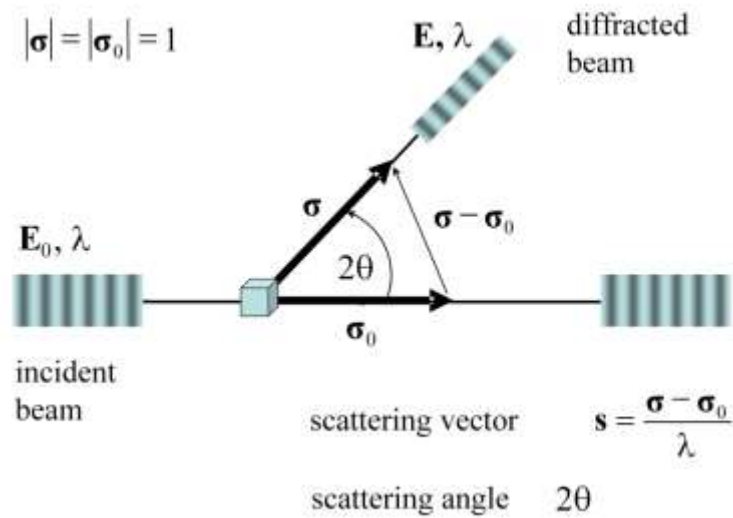


Fig. 1. A scheme of an X-ray diffraction experiment (the figure is reproduced from [1]).

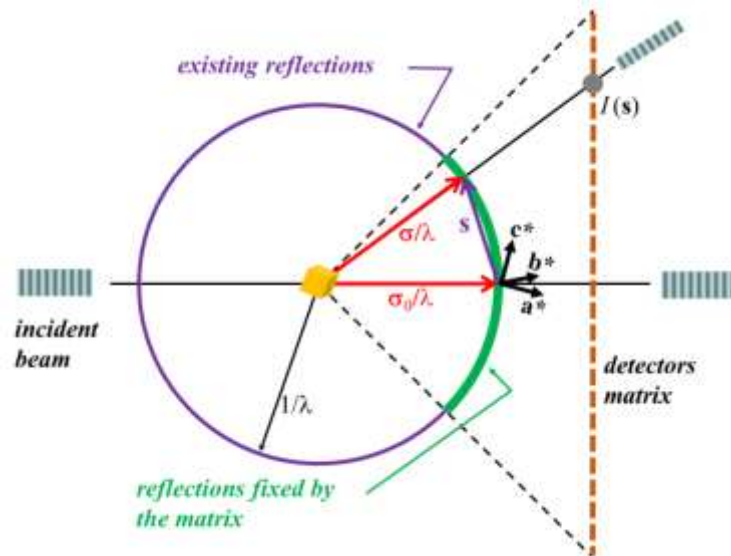


Fig. 2. The Ewald scheme of the diffraction experiment. The scattering vectors  $\mathbf{s}$  that correspond to the reflections existing at a given time form the surface of a sphere (the Ewald sphere) in the reverse space (shown in purple). The reflections registered by the detector correspond to the part of this sphere (shown in green) determined by the physical dimensions of the detector matrix. The rotation of the object is accompanied by the rotation of the basis of the inverse space  $\{\mathbf{a}^*, \mathbf{b}^*, \mathbf{c}^*\}$ , i.e., a change in the position of the Ewald sphere and the scattering vectors of the registered reflections in the inverse space (the figure is reproduced from [1]).

In the framework of the kinematic scattering theory, the processes that occur can be described as follows [2, 3]. The periodically changing electric field of the incident wave causes the electrons of the object under study to oscillate. The oscillating electrons become the sources of spherical electromagnetic waves, which are summed up on the detector. In this summation, the key role is played by the phase differences of the waves coming from different electrons, which, in turn, are determined by the relative position of electrons in the object. The relative position of electrons in the object is described by the electron density

distribution  $\rho(\mathbf{r})$  so that the number of electrons in the elementary volume  $dV$  centered at the point  $\mathbf{r}$  is  $\rho(\mathbf{r})dV$ . The computational task of the X-ray diffraction analysis is to find the distribution  $\rho(\mathbf{r})$  based on a set of X-ray images collected in the experiment. The electron density distribution found can be further interpreted in terms of a set of atoms whose coordinates are further refined [4].

Depending on the problem to be solved, the X-ray beam is considered either as a plane sinusoidal electromagnetic wave characterized by the wavelength  $\lambda$  and the amplitude of the primary electromagnetic wave  $E_0$ , or as a photon flux characterized by the energy of the photon  $E_{\text{photon}}$  and the photon flux density  $j$  (the number of photons passing through a unit area per unit time). The length and amplitude of the wave are related to the energy and density of the photon flux by the relations

$$E_{\text{photon}} = \frac{hc}{\lambda}, \quad j = \frac{\lambda}{8\pi h} E_0^2, \quad (1)$$

where  $c$  is the speed of light and  $h$  is the Planck's constant. These relationships allow one to move from one type of description to another if necessary. When solving the structure, i.e., determining the positions of atoms based on the result of the X-ray experiment, a wave description is used. When we are talking about the parameters of the devices that generate X-rays, or about the processes of radiation damage of the object, the corpuscular description is more convenient.

## 1.2. Mathematical description of the results of a diffraction experiment. Structure factors

Let vector  $\boldsymbol{\sigma}_0$  (of unit length) indicate the direction of the primary X-ray beam, and the unit vector  $\boldsymbol{\sigma}$  be directed from the object to the point of the energy registration of the secondary beam (the pixel in the matrix of detectors). In the framework of the kinematic scattering theory, the energy of a secondary beam  $E(\boldsymbol{\sigma}_0, \boldsymbol{\sigma})$  scattered by the object with the electron density distribution  $\rho(\mathbf{r})$  can be represented as

$$E(\boldsymbol{\sigma}_0, \boldsymbol{\sigma}) = \varepsilon E_0 |\mathbf{F}(\mathbf{s})|^2. \quad (2)$$

Here,  $E_0$  is the energy of the primary wave, and the constant  $\varepsilon$  is a combination of physical constants and experimental parameters (e.g., the distance from a sample to the detector and the time of the exposure to X-rays) and does not depend on the structure of the sample. Vector  $\mathbf{s}$  is the wavelength-normalized combination of the vectors that determine the directions of the primary and secondary rays

$$\mathbf{s} = \frac{\boldsymbol{\sigma} - \boldsymbol{\sigma}_0}{\lambda}. \quad (3)$$

This vector plays an important role in the scattering theory and in crystallography, and is referred to as the scattering vector (an alternative name in other sections of physics the transmitted momentum vector). Complex quantities  $\mathbf{F}(\mathbf{s})$  in crystallography are called structure factors and are calculated as

$$\mathbf{F}(\mathbf{s}) = \int_{\mathbf{R}^3} \rho(\mathbf{r}) \exp[i2\pi\mathbf{s} \cdot \mathbf{r}] dV_{\mathbf{r}}, \quad \mathbf{s} \in \mathbf{R}^3, \quad (4)$$

where  $\mathbf{s} \cdot \mathbf{r}$  denotes the scalar (dot) product of vectors  $\mathbf{s}$  and  $\mathbf{r}$ . The squares of the magnitudes of these quantities  $I(\mathbf{s}) = |\mathbf{F}(\mathbf{s})|^2$  are called intensities of reflections.

### 1.3. Reconstruction of the electron density distribution. Phase problem. Resolution

Integral (4) is nothing but the Fourier transform of the electron density distribution  $\rho(\mathbf{r})$ . Therefore, the electron density distribution can be calculated as the inverse Fourier transform:

$$\rho(\mathbf{r}) = \int_{\mathbf{R}^3} \mathbf{F}(\mathbf{s}) \exp[-i2\pi\mathbf{s} \cdot \mathbf{r}] dV_{\mathbf{r}}, \quad \mathbf{r} \in \mathbf{R}^3, \quad (5)$$

provided that the complex values  $\mathbf{F}(\mathbf{s})$  are known for all vectors  $\mathbf{s}$  in the three-dimensional space. (In crystallography, the space of scattering vectors is called the reciprocal space). In practice, the implementation of formula (5) faces two fundamental problems.

The first problem, the so-called "phase problem", is that the values of both magnitudes and phases of complex structure factors are necessary for the calculation of  $\rho(\mathbf{r})$  by formula (5). At the same time, as follows from formula (2), the standard diffraction experiment allows one to determine (on a relative scale) only the values of magnitudes  $|\mathbf{F}(\mathbf{s})|$  of the structure factors. The recovery of phase values  $\varphi(\mathbf{s})$  is a central computational problem in biological crystallography. A number of approaches are used to solve this problem, and none of them is universal [5–7].

The second problem is related to the fact that the calculation by formula (5) requires knowledge of all structure factors, while, in practice, even magnitudes can be determined only for a part of them. The completeness of the set  $\mathcal{S}$  of scattering vectors included in the calculation of integral (5) is usually characterized by the value of "resolution". The concept of "resolution" has various interpretations in crystallography and is discussed in a number of papers [8–10]. We will limit ourselves here to the main concept, the concept of "formal resolution". Formula (5) represents the electron density distribution as the sum of Fourier harmonics  $\exp[-i2\pi\mathbf{s} \cdot \mathbf{r}]$  weighted by the values of structure factors. The real and imaginary parts of this complex function are functions that vary sinusoidally along the direction  $\mathbf{s}$  and do not change in planes perpendicular to this direction. (Such functions can be called "standing plane waves"). The period of the function along the direction  $\mathbf{s}$  is equal to

$$d = \frac{1}{|\mathbf{s}|} = \frac{\lambda}{2 \sin \theta}, \quad (6)$$

and is called the resolution corresponding to the reflection  $\mathbf{s}$  and the structure factor  $\mathbf{F}(\mathbf{s})$ . Here  $\theta$  is half the angle value between the directions  $\boldsymbol{\sigma}$  and  $\boldsymbol{\sigma}_0$ , and  $\lambda$  is radiation wavelength. A set of reflections  $\mathcal{S}$  is said to be of the resolution  $d_{\min}$  if all (or "almost all") reflections with  $|\mathbf{s}| \leq d_{\min}^{-1}$  are included in it. Integral (5) calculated from this set of reflections is called the Fourier synthesis of the electron density resolution  $d_{\min}$ . The value of  $d_{\min}$  determines the minimum size of the details that are distinct on "topographic maps" corresponding to this Fourier synthesis.

### 1.4. Possibility of experimental measurement of the intensities of the reflections. Crystals

The main problem in performing of the experiment described above is the extreme weakness of scattered X-rays. The value of the constant  $\varepsilon$  in equality (2) can be estimated as  $10^{-24}$ , which makes it extremely difficult to register scattered rays. The whole history of the development of X-ray diffraction analysis is related with the search for the ways to overcome this problem. The most obvious ways to solve this problem are the follow.

- **An increase in the power of X-ray source** (an increase in the value  $E_0$  in formula (2)). Until recently, synchrotrons were the most powerful source of X-ray radiation. Recently developed X-ray lasers are significantly more powerful radiation sources.

- **An increase in the sensitivity of the detector.** Most modern detectors allow one to record individual X-ray photons [11].
- **An increase in the exposure time of the X-ray image.** The applicability of this approach is limited by the destruction of biological macromolecules by X-ray radiation. We will discuss this issue in more detail in Section 3 below.
- **A collection of a diffraction pattern from several samples.** Speaking about the radiation damage to a sample, it should be taken into account that, during the experiment, it is necessary to obtain a set of diffraction images. This means that only a fraction of the total radiation resource of the object can be used to obtain each of them. This problem can be partially mitigated by a sequential data collection from multiple identical copies of the object. Further development of this idea is the “flow” (serial) scheme of the organization of the experiment, when each X-ray image is obtained from a separate copy of the object. We will discuss this in more detail in section 2.1.1.

Despite constant progress in the development of experimental techniques at all stages of experiment, it was impossible, until recently, to obtain a diffraction pattern from a single biological macromolecule.

So far the only way to bypass the problem of impossibility to detect weak rays is to prepare an experimental sample in the form of a single crystal. In a crystal, a set of identical equally oriented macromolecules are arranged in a regular way so that equivalent points of different molecules fill the three-dimensional periodic lattice. Let  $\{\mathbf{a}, \mathbf{b}, \mathbf{c}\}$  be the minimal linearly independent periods (basis) of this lattice. Secondary waves coming to the detector from different copies of the molecule have phase shifts that are multiples of  $2\pi\mathbf{s} \cdot \mathbf{a}, 2\pi\mathbf{s} \cdot \mathbf{b}, 2\pi\mathbf{s} \cdot \mathbf{c}$ . In the case that the conditions of Bragg – Wolfe are satisfied

$$\mathbf{s} \cdot \mathbf{a} = h, \mathbf{s} \cdot \mathbf{b} = k, \mathbf{s} \cdot \mathbf{c} = l, \quad h, k, l - \text{integer}, \quad (7)$$

all waves come with equal phases. In this case, the intensity of the total wave on the detector increases by a factor of  $N^2$ , where  $N$  is the number of molecules in the crystal sample. This radical increase in the intensity makes it possible for the detector to register the wave, and these reflections are called Bragg reflections. If the conditions (7) are not met, the waves come with different phases and suppress each other. Thus, the crystal plays a dual role. On the one hand, it dramatically amplifies the signal for a discrete set of reflections defined by equations (7) and, on the other hand, it suppresses information for the rest of the reflections.

If a crystal is used as a sample, the electron density distribution in it is periodic in three independent directions, and integrals (4) and (5) take the form of the Fourier series

$$\mathbf{F}(\mathbf{s}) = \int_V \rho(\mathbf{r}) \exp[i2\pi\mathbf{s} \cdot \mathbf{r}] dV_r \quad (8)$$

$$\rho(\mathbf{r}) = \frac{1}{|V|} \sum_{hkl-\text{целье}} \mathbf{F}(\mathbf{s}_{hkl}) \exp[-i2\pi\mathbf{s}_{hkl} \cdot \mathbf{r}], \quad (9)$$

where  $V$  is a unit cell (a parallelepiped built on vectors  $\{\mathbf{a}, \mathbf{b}, \mathbf{c}\}$ ),  $|V|$  is its volume,  $\mathbf{s}_{hkl}$  is a vector defined by equations (7) for the given values of the indices  $hkl$ .

The preparation of the crystal of the object under study is the most difficult part of X-ray diffraction research, which is not always implemented in practice.

## 2.1. The main directions of research in structural biology with the use of free electron lasers

### 2.1.1. Serial crystallography

A significant advantage of X-ray lasers over synchrotrons is a high concentration of radiation energy in the region of the intersection of the X-ray beam with a sample, which makes it possible to obtain diffraction patterns for very small crystals with the size of several microns. This opens up possibilities, in particular, for determining the structure of membrane proteins. Due to a low level of expression, difficulties with purification, and the instability, it is difficult to obtain membrane proteins of good quality in necessary quantities to grow crystals large enough for X-ray crystallography.

In a traditional crystallographic experiment at a synchrotron, a single crystal mounted on a goniometric head is rotated between exposures, which, ideally, makes it possible to measure a full set of diffraction intensities. During each exposure, the crystal rotates at a small angle in order for the full intensities of individual Bragg reflections to be measured. In serial crystallography experiments, a stream of crystals is delivered into X-ray pulses. A crystal caught in an X-ray pulse gives only one diffraction image containing partially exposed Bragg reflections. To obtain a complete set of experimental data, a huge number of diffraction images have to be collected, processed, and combined into a single set [15].

The first serial experiments were conducted at LCLS with microcrystals of the large membrane protein complex of photosystem I [16]. The crystal sizes in these experiments ranged from 200 nm to 2  $\mu\text{m}$ . The structure of photosystem I in these experiments was determined at a resolution of 8  $\text{\AA}$ , which was limited by the incident beam wavelength of 6.9  $\text{\AA}$ . Later, the first experiments with protein crystals with sizes of the order of several microns were carried out; the data of atomic resolution up to 1.9  $\text{\AA}$  were obtained [17]. During the following years, femtosecond flow crystallography experiments were performed with large complexes, such as photosystem II and ribosomes [18–20], as well as with g-protein coupled receptors [21, 22] and a number of soluble and membrane proteins [23–25]. Currently, the smallest crystals used for diffraction experiments at LCLS (and at all X-ray lasers) the diffraction data from which were collected to a relatively high resolution of 1.9  $\text{\AA}$  are the native crystals of the occlusion bodies of *Cydia pomonella* granulovirus [26]. The volume of crystals delivered into the X-ray pulse was on the average 0.016  $\mu\text{m}^3$ , which is approximately equal to 9000 elementary crystal cells.

With the commissioning of EuXFEL, the term megahertz crystallography appears, which has the same meaning as serial femtosecond crystallography but implies a higher pulse repetition rate. The first serial experiments at EuXFEL were performed with crystals of small proteins concavalin A, concavalin B, and beta-lactamase [27, 28]. In these experiments, data were collected up to a resolution of 1.7 and 2.1  $\text{\AA}$  and the possibility of determining crystalline protein structures from EuXFEL data was shown. In recent experiments with microcrystals of photosystem I of cyanobacteria (the size of the crystals  $5 \times 5 \times 15 \mu\text{m}^3$ ) the crystal structure of photosystem I was determined at a resolution of 2.9  $\text{\AA}$  [29].

It should be noted that the term serial crystallography is also used in the literature in a different sense when it comes to determine a series of structures that correspond to different states of the object under study.

### 2.1.2. The study of fast processes (time-resolved crystallography)

At the moment, significant progress in this area has been made using so-called pump-probe experiments, in which an optical laser (“pump”) excites the object under study (transfers it into a different state), and an X-ray laser examines it (“probe”). Objects under study are biological molecules that, under the influence of light, pass into short-lived transition states accompanied by structural changes in their structure [30–36]. In the experiment, for a fixed time before the samples fall into the X-ray laser beam and diffraction

data are recorded, the samples are irradiated with a light source (optical laser), thereby initiating the reaction and corresponding structural changes in the sample. The experiment is carried out at different times of delay between the action of the optical laser and the hit of samples by the X-ray pulse. The diffraction experiment is also performed for the samples that have not been irradiated with the optical laser (in the so-called “dark state”, “dark probe”). After processing the diffraction data and building the models of structures, researchers get a set of spatial structures corresponding to different times that have passed since the beginning of the reaction, and, therefore, have the opportunity to study the structural changes occurring with time. The reason why these changes are difficult to study at synchrotrons is that the minimum duration of an X-ray pulse on a synchrotron is of the order of 100 ps. Structural changes caused by the breaking of bonds occur at much shorter times (on the femtosecond scale), and X-ray lasers in long-term perspective are a powerful tool for studying them. Examples of these studies are the investigations of myoglobin and photoactive yellow protein (PYP).

Myoglobin is a protein that stores oxygen in muscles and imparts red color to them. Along with the polypeptide chain, a myoglobin molecule has a heme containing  $\text{Fe}^{2+}$  ion with which ligands, such as CO, easily bind. The covalent bond between  $\text{Fe}^{2+}$  and CO is broken by light within 50 fs. In an experiment conducted at LCLS, diffraction data for myoglobin crystals were obtained at ten delay times between the flash of the optical laser and the entry of the crystal into the laser pulse (from 0.1 to 150 ps) [33]. Based on the diffraction data, structural changes in the heme and the surrounding part of the protein were studied.

The photoactive yellow protein (PYP) is a small water-soluble protein that contains a covalently bound chromophore (para-coumaric acid). The absorption of a photon from the blue region of the spectrum triggers a complete photocycle, a sequence of reactions and structural changes the first of which is the cis-trans isomerization of the chromophore. In the experiments conducted at LCLS and a synchrotron, diffraction data were obtained with a delay between the optical laser and the X-ray pulse of 3 and 100 ps, respectively [34]. In recent experiments at EuXFEL, the researchers were able to collect data for three intermediate points on the time scale, with a delay between the optical and the X-ray lasers of 10, 30 and 80 ps, and, thus, obtain dynamic structural data in the range that has not been studied previously [36]. Thus, detailed structural changes of the chromophore isomerization process can be studied at the smaller time step.

### 2.1.3. Experimental studies of single particle

In structural biology, a “single particle” is defined as a separate biological object that is not in a crystalline state, for example, a separate cell, a separate viral particle, or a separate protein molecule. At modern synchrotrons, the intensity of X-ray diffraction from these objects is too weak to be measured. Therefore, the commissioning of such high-intensity radiation sources as XFEL creates a hope to extend the X-ray diffraction analysis methods to individual macromolecular particles [37]. In the subsequent text, we will focus mainly on the problems of the implementation of this approach in practice.

## 3. RADIATION DAMAGE TO OBJECTS IN EXPERIMENTS AT X-RAY LASERS

### 3.1. Diffraction before destruction

The use of super-intensive and ultra-short pulses of free-electron lasers to obtain diffraction data for single non-crystalline biological samples was proposed even before X-ray lasers were put into operation, and was one of ideas that motivated their construction. A pulse of X-ray laser has such a high intensity, which is of the orders of magnitude higher than that of the radiation of modern synchrotrons, so that the diffraction signal from a non-crystalline sample will be high enough to register it. However, a laser pulse of such high power can cause a destruction and an explosion of the sample. It was suggested that for very short pulse

durations, in the ideal case, less than 10 fs, it would be possible to register the diffraction pattern before the sample is destroyed [38]. This diffraction pattern is called “diffraction before destruction”.

### 3.2. Destruction of a sample by an X-ray pulse

When an X-ray beam passes through a sample, both elastic beam scattering (Thompson scattering), which contributes to the diffraction pattern, and inelastic scattering (photoelectric effect and Compton effect), during which all or part of the photon energy is transferred to the sample atoms, occurs. The energy absorbed by the sample is used for knocking out electrons from atoms and the subsequent ionization of atoms, for propagation of electrons through the sample, for the breakage of covalent bonds, fluorescent emission, and the heating of the sample.

Radiation damage to a sample begins with the absorption of an incoming photon by an atom, which is accompanied by the emission of a photoelectron from the atomic K-shell with an energy from several hundred to thousands of electron volts [39, 40]. Then, the transition of an electron from the outer shell to a vacant place on the inner shell in the atom (Auger transition) and either the emission of Auger electron [41, 42] or fluorescent radiation take place (for light atoms, the emission of Auger electron is more probable). The Auger transition time in biomolecules ranges from 4.9 fs for oxygen to 10.7 fs for carbon [43]. Photoelectrons and Auger electrons have significantly different energy and velocity values. For example, if the energy of the absorbed photon is 6 keV, the initial speed of the photoelectron of a carbon atom is 450 Å/fs, while, for the Auger electron, it is 100 Å/fs [40]. Photoelectrons and Auger electrons propagate through the sample, interact with the atoms of the sample, and cause cascades of secondary ionization in the time range from 10 to 100 fs [44]. An electron with an initial energy of 5.7 keV causes 240 secondary ionization events within 10 fs [40]. Ionization of atoms causes changes in atomic form factors and Coulomb repulsion of ionized atoms, which leads to their shift, or, more precisely, repulsion from each other [41, 45]. Simultaneously with the Coulomb expansion, the phenomenon of electron capture occurs, when negative charges can no longer escape from the system, causing, on the one hand, the neutralization of the positive charge of the system, and, on the other, a further increase in the ionization rate [38, 41, 46]. All these processes will cause attenuation and an increase of the level of noise of the diffraction pattern. A high degree of ionization of the sample leads to a Coulomb explosion and its complete destruction [38, 47, 48].

In modern free-electron lasers, the pulse energy reaches 4 mJ, and the number of photons per pulse can be as large as  $10^{12}$ . The pulse duration ranges from several fs to several tens of fs. For example, if the beam is concentrated on an area of one  $\mu\text{m}^2$ , this gives a photon flux density of up to  $10^4/\text{\AA}^2$  per pulse. To study single particles, the so-called nano-focusing of beams is used to obtain diffraction patterns containing as many photons as possible (when the diameter of the focused beam is less than one  $\mu\text{m}$ ). This leads to even higher density of the photon flux that falls on the sample and an increase in the diffraction signal, but this will also cause an increase in radiation damage.

Among the most important issues in the organization of a specific experiment are:

- Under what conditions does Coulomb explosion start, i.e., how to plan an experiment to get a diffraction pattern before Coulomb explosion of the sample?
- Under what experimental conditions will the level of the diffraction signal significantly exceed the noise level caused by the destruction of the sample during the pulse?

### 3.3. Radiation dose as a characteristic of the degree of the radiation damage to the sample

The transfer of energy to the sample and, accordingly, the degree of its destruction are quantified using a physical quantity called the radiation dose (or simply the dose). The dose is

the energy absorbed by the sample during the interaction of incoming X-ray radiation with the sample per unit mass of the sample. The dose is measured in gray (Gy). One gray equals one Joule divided by 1 kg of mass. The dose can be estimated by the formulas:

$$Dose = I_{incident} \left(1 - \exp\left(-(\mu/\rho)\rho x\right)\right) / m$$

$$\mu/\rho = (n_C\sigma_C + n_N\sigma_N + n_O\sigma_O + \dots) / \rho \quad , \quad (10)$$

$$I_{incident} = Flux E_{ph}$$

where  $I_{incident}$  is the total energy of the incident beam that falls on the sample,  $m$  is the mass of the irradiated part of the sample,  $Flux$  is the flux of the photons that fall on the sample,  $E_{ph}$  is the energy of one photon,  $\mu/\rho = \sigma n/\rho$  is the mass absorption coefficient,  $n$  is the number of atoms of a specified type per unit volume (C, N, O – chemicals),  $\sigma$  is the interaction cross section for a given type of atoms,  $\rho$  is the density of the sample, and  $x$  is the thickness of the sample. For specific samples, the mass absorption coefficient is either calculated using tabulated cross-section values for different chemical elements (for example, using International Tables for Crystallography or using the server <https://physics.nist.gov/PhysRefData/Xcom/html/xcom1.html>), or is measured in an experiment [49]. The radiation dose can also be calculated using the program RADDPOSE-3D [50, 51] or a recently improved version of this program RADDPOSE-XFEL for experiments on free electron lasers [52].

In protein crystallography, an estimate for the dose limit, the so-called Henderson limit, equal to  $30 \cdot 10^6$  Gy is widely used (sometimes in the literature, the Henderson limit is taken to be  $20 \cdot 10^6$  Gy). Initially, this estimate was obtained as a dose value for medium-sized crystals at which radiation damage causes a decrease in the diffraction intensity by approximately two times. Later, the value of the Henderson limit was proposed based on numerous experimental data as the recommended dose limit in experiments on synchrotrons with medium-sized crystals at 100 K [53]. For experiments at room temperature at synchrotrons, an estimate of  $0.38 \cdot 10^6$  Gy for the recommended dose limit [54] was recently obtained.

However, in experiments with single particles, these estimates for the dose limits appear to be not valid. Even in the first experiments with single particles on synchrotrons, no signs of sample destruction in the diffraction patterns at doses significantly exceeding the Henderson limit were detected [55–57]. For example, in the experiments with a single cell, the total dose absorbed by the sample during the experiment was estimated to be  $455 \cdot 10^6$  Gy, which is an order of magnitude higher than the Henderson limit [56]. In experiments using SACLA, in which diffraction patterns were obtained and a two-dimensional reconstruction of a single cell was made, the dose per pulse was estimated to be  $100 \cdot 10^6$  Gy [58]. Thus, both in synchrotron and free-electron laser experiments, diffraction data were collected at doses significantly exceeding the previously determined maximum possible values.

### 3.4. Reliability of the maximum possible dose estimate

Let us consider possible reasons for the discrepancy between the theoretical and experimentally obtained estimates of the maximum possible dose.

When analyzing the reasons why generally accepted maximum possible dose estimates are not valid in experiments with single particles, we must first take into account that almost all diffraction data from single particles have been obtained at a very low resolution, of the order of tens of nanometers. While the recommended dose limits (Henderson limit, etc.) were obtained with crystals at an average resolution of about 2 Å. The higher the resolution of the data, the more sensitive they are to radiation damage [57, 59, 60]. The fact that, in the experiments of Rodriguez and co-authors, the cells were resistant to the high dose and the diffraction pattern did not change (Fig. S2, [56]) most likely can be explained by the very low resolution of the diffraction patterns, which did not exceed 50 nm. Although the total dose of

$4.55 \cdot 10^8$  Gy received by the cell in the experiments exceeded the Henderson limit by an order of magnitude, this value is apparently not enough for a significant damage to the cell that would cause distortions of the diffraction pattern at a resolution of 50 nm. For example, in the case that the maximum resolution value lies in the range of 0.1–10 nm, an empirical formula was proposed that relates the resolution value of the diffraction pattern in nanometers to the maximum dose value in Gy that the sample can withstand:  $\text{Dose} = 10^8 \cdot \text{Resolution}$  [57].

In synchrotron experiments, the low resolution of the data seems to be the main reason why the radiation damage does not significantly affect the diffraction pattern.

The second point that one has to take into account is the differences in the parameters of the incident beam between a synchrotron and a free electron laser. At free electron lasers, the photon flux density reaches  $10^4$  ph/Å<sup>2</sup> per pulse (i.e., per tens of fs), while, for example, in experiments with a single cell at a synchrotron, the photon flux density per diffraction image was estimated as 0.5 ph/Å<sup>2</sup> per second [57]. The intensity of the incident beam at a modern X-ray laser is many orders of magnitude higher than the intensity at synchrotrons. Accordingly, the values of the doses received at an X-ray laser are also very high in comparison with those at synchrotrons. Already in the first experiments with crystals at X-ray lasers, estimates from  $700 \cdot 10^6$  Gy to 3 GGy for a dose per pulse were obtained [16, 61]. At the same time, the solved structures did not contain any signs of radiation damage observed in crystal structures on synchrotrons. These experimental results on lasers were interpreted as confirmation of the possibility of “diffraction before destruction”.

The dose obtained by a sample on X-ray lasers is orders of magnitude higher than the dose obtained in synchrotron experiments. And this dose is obtained in a much shorter time, in tens of femtoseconds, while on synchrotrons, collecting only one frame can last seconds. In data collection on synchrotrons, radiation damage accumulates over a much longer time interval than the duration of the laser pulse. With the accumulation of experimental results, more accurate estimates for the maximum possible dose values in laser experiments will apparently be obtained.

In the case of a single particle, to obtain a precise estimate for the dose value is quite a challenge. A single biological particle (cell, virus, and organelle) is much smaller than the smallest crystals. When estimating the dose, it is necessary to carefully determine the number of photoelectrons and Auger electrons that will leave the sample instead of spreading through the sample and causing a cascade of new reactions and a further destruction of the sample. Taking this fact into account can significantly reduce the estimate for the absorbed dose (Fig. 8 in [51]).

The number of experimental studies of chemical and structural processes in samples caused by an X-ray pulse over a period of about tens of femtoseconds is not yet high due to the facts that the X-ray lasers just start to be commissioned, the process of debugging them is underway, and the experiment is complex. The first experimental studies of the effects of ionization and charge redistribution caused by an X-ray laser pulse were carried out with small molecules containing a heavy atom [62–66]. Molecular fragmentation caused by Coulomb explosion was studied for small molecules containing iodine atom [67–69] and for the relatively large C60 molecule [70, 71].

At the same time, particular studies began to appear that contained experimental evidence that at high values of the photon flux density, which are achieved due to nano-focusing of the beam, or at relatively long laser pulses, global and local damage of protein crystals is observed, similar to one that occurs in crystal structures on synchrotrons. Initially, these phenomena were detected only for relatively long pulses. For example, a decrease in the diffraction intensity was detected at a high resolution for a pulse length of 70 fs [61]. Local destructions were observed at a pulse length of 40 fs [72]. Changes in the electron density for metal atoms or ions, sulfur atoms, structural changes in the region surrounding the cluster with heavy atoms [72–74], elongation of disulfide bonds, and structural changes in the side groups of aromatic residues were reported [75].

In many recent studies along this line, a “pump-probe” scheme of the experiment (used at modern lasers) is applied, in which two laser pulses fall onto a sample at a fixed time interval. The first pulse initiates the damage to the sample, and the second pulse is designed to obtain a diffraction pattern from the sample in which these destructions have already begun to occur between the two pulses [75, 76]. Note that in the recent study, local effects of radiation damage in crystals were observed already at time intervals between pulses approximately equal to 20–30 fs [75].

Studies of this type have not yet been carried out with single biological molecules. The fact of obtaining X-ray images from individual particles and the fact that two- or three-dimensional models of the particle were built using these data are considered by many researchers as a confirmation of the possibility to obtain the diffraction before destruction. However, we emphasize once again that, at a very low resolution, we can only state that the diffraction was obtained before the Coulomb explosion, but we cannot judge the degree of destruction of the sample. Almost all diffraction data obtained for single particles were obtained at a resolution of the order of tens of nanometers, with the exception of the data for the tobacco mosaic virus, which were collected at a resolution of 5.9 Å [77]. However, we note that the structure of the virus was solved only at a much lower resolution of 69–72 Å [78].

The first results of modeling of ionization and Coulomb explosion of a single protein molecule on a future free-electron laser were reported in the paper where the idea of diffraction before destruction was proposed [38]. The lysozyme molecule surrounded by 118 water molecules was taken as a sample. Pulses of different duration, from 2 to 50 fs, were modeled. The Coulomb explosion always occurred (during or, in some cases, after the pulse) (Fig. 2 from [38]). We emphasize that, along with the number of photons per pulse, one of the key parameters when modeling damage processes is the photon flux density, which is equal to the photon flux per unit area. The value of the photon flux per pulse was taken as  $10^{12}$ , which corresponds to the value achieved with modern lasers, while, the value of the photon flux density of  $3.8 \cdot 10^6$  ph/Å<sup>2</sup> at which these calculations were performed, exceeds the maximum value currently achieved in experiments with single biological particles. In subsequent works, Coulomb explosion was reproduced many times in computer simulations [79, 80].

The parameters of the incident beam that directly define the degree of radiation destruction of the sample are the photon flux density and the pulse duration. In experiments with single molecules, it is desirable that the photon flux density of the incident beam be as high as possible. However, the radiation damage will, then, also be significant. The radiation damage can be reduced if the pulse duration is less than the Auger transition time [38, 46, 81]. In this case, the ionization level of the sample will be significantly lower, and diffraction will occur before the secondary ionization cascades propagate. For a carbon atom, the Auger time is 10 fs, and for a sulfur atom, it is 1.3 fs [82]. Fortmann-Grote and colleagues concluded that, in experiments with single particles, the optimal pulse duration should be between three and 9 fs, and 9 fs is the preferred time, since the diffraction signal in this case will contain a much large number of photons, which is important at the next step for determining the particle orientation [39]. Previously, it was suggested that, radiation destruction can be prevented by using a pulse lasting several hundred attoseconds [83]. At the moment, this pulse duration is not yet achievable.

However, there are results that are more optimistic. Numerical simulations of the interaction of an X-ray pulse and a single lysozyme molecule were performed at  $10^{12}$  and  $10^{13}$  photons per pulse [80]. The diameter of the focused beam was assumed to be 100 nm, which gives the values for the photon flux density of the order of  $10^6$  and  $10^7$  ph/Å<sup>2</sup>. Note that such high photon flux density values have not yet been achieved at modern lasers. Based on numerical experiments, the authors concluded that for pulses with a duration not exceeding 50 fs, the radiation damage is insignificant and its effect on the diffraction image does not exceed the effect of the sample inhomogeneity. In [84], the influence of non-stationary atomic

scattering factors in a high-power X-ray beam on the intensities of rays scattered by biological macromolecules was studied by computer modeling methods. It was found that the changes in the diffraction pattern caused by the time dependence of the scattering factors are negligible if the photon flux density in the primary beam does not exceed  $10^4$  ph/Å<sup>2</sup> during the pulse, which corresponds to the power of modern X-ray lasers. However, if the photon flux density increases to  $10^6$  or  $10^8$  ph/Å<sup>2</sup> per pulse, the discrepancies become significant and require corrections to the schemes of the theoretical calculation of the diffraction pattern.

#### 4. ORGANIZATION OF AN EXPERIMENT IN STUDIES OF MACROMOLECULAR OBJECTS USING FREE ELECTRON LASERS

##### 4.1. Delivery of samples into an X-ray beam

Not all X-ray laser stations have appropriate conditions for experiments with single particles. (Relevant information is on the website of each laser). For example, at LCLS, it is possible to conduct these experiments at two stations, Coherent X-ray Imaging (CXI) and Atomic, Molecular & Optical Science (AMO). Experiments with single particles at EuXFEL are currently conducted at SPB/SFX station. The first demonstration of the possibility of diffraction data collection from a single non-crystalline solid sample on free electron lasers and the determination of its structure was performed at FLASH [85]. The first experiment with a biological sample (mimivirus) was carried out at the AMO station of the LCLS [86]. Further experiments with single biological samples (individual cells, cell organelles, bacteria, and viruses) were performed using LCLS, SACLA, and EuXFEL. The key points for organizing these experiments, along with the support of the radiation source and the very complex equipment at the stations, are the availability of a sufficient number of approximately identical samples of individual particles and an effective delivery of samples into the X-ray beam. The requirement of "identity" of the samples is caused by the fact that one two-dimensional diffraction pattern (image, frame) is recorded for each sample. The presence of a large number of two-dimensional diffraction patterns from approximately identical objects that correspond to different orientations of the object relative to the X-ray beam allows one to hope that it will be possible, by combining all these data, to determine the three-dimensional structure of the object. Methods for delivering samples into the X-ray beam are currently being tested and improved.

##### 4.1.1. Delivery of samples in aerosol form

In single-particle experiments on free-electron lasers, samples are currently delivered into the beam in two ways: in the form of an aerosol (at the moment of intersection with the laser pulse, samples are in the gaseous phase) and on fixed targets (samples can be either in the liquid substrate or in the solid state). In most experiments, samples are supplied as an aerosol [86–92]. With this method of delivery, the goal is to isolate the particle under study from the surrounding liquid solution. The intensity of the diffraction signal is the sum of the signal from the particle and the signal from the surrounding medium in which it is delivered to the X-ray beam. The signal from a single non-crystalline particle is relatively weak even at pulse flux densities as high as in free-electron lasers. It is significantly weaker than the signal from crystals and may be weaker than the signal from a solvent. In the aerosol delivery method, the solvent evaporates before the particle enters the X-ray beam. Thus, the particle does not have a liquid environment that contributes to scattering and that makes it difficult to determine the diffraction signal from the particle itself.

A general scheme of sample delivery, in this case, includes the transfer of the samples from the buffer solution to the state of aerosol droplets, the delivery of the droplets to a vacuum chamber, where the droplets evaporate and, after which individual particles are focused by aerodynamic lenses at the intersection with the X-ray pulse.

Aerosol droplets are formed either via an aerodynamic nozzle (gaz-dynamic virtual nozzle, GDVN [93]) using helium or by electrospray [94, 95]. The GDVN nozzle allows one, using a gas stream, to compress the liquid jet with samples up to several micrometer. When using an electrospray, the flow of particles from the solution is formed under the influence of only electrostatic forces. The injector, created at the Uppsala University, allows the delivery of single particles of sizes from 30 to 3000 nm. The speed of incoming particles depends on their size and the gas flow rate. For example, particles smaller than 100 nm have a speed of up to 200 m/s, while particles of the order of a micrometer have a speed of no more than 20 m/s [96].

In most single-particle experiments, GDVNs were used. Relatively recently, it was proposed, as an alternative, to use electrospray for forming aerosol droplets [97]. The authors performed experiments at LCLS with several different biological samples (carboxysomes, tbsv tomato virus, and Rubisco protein). It was shown that electrospray allows one to increase the speed of droplet delivery by approximately 15 times compared with the delivery of particles by GDVNs, as well as to obtain aerosol drops of smaller sizes and with a smaller spread of sizes for sucrose and biological samples. A higher delivery speed can provide a higher frequency of X-ray beam hits of the particles, and a smaller size of aerosol droplets provides less contaminations on the surface of aerosol droplets. Aerosol droplets have a size of the order of a micron or less and contain a different number of test particles (each drop can contain from zero to several particles).

If samples are delivered in the form of an aerosol, there are a number of fundamental difficulties that have to be taken into account at the next stages of the structure determination:

- After the evaporation of droplets containing several particles, clumped particles can be formed, i.e., an aggregation of the samples can occur, and, either one or several clumped particles can enter the beam.
- Non-volatile chemical compounds from the solution settle on the surface of aerosol droplets, which leads to an additional noise and a distortion of the diffraction data.
- The number of hits of the laser pulse on the particles is relatively low, which makes it necessary to prepare a very large number of samples (for example, it took 10 months to prepare samples for one night shift of data collection with EuXFEL, private communication).

Work is currently in progress to improve the design of aerosol injectors. The main directions of the improvement of aerosol injectors include increasing the number of laser beam hits on particles, reducing residual gas (for example, helium or carbon dioxide) in the vacuum chamber, which leads to the noise of the diffraction data, and elimination of breakage of the injector.

#### 4.1.2. Delivery of samples on solid targets

In several experiments with single particles on synchrotrons, samples were fixed and delivered into the beam on solid targets [56, 98, 99]. The experiment in this case was a modification of the standard X-ray crystallographic experiment. Either a sample was mounted on a goniometric head and rotated during the exposure [56] or only one diffraction pattern was taken for each sample [98].

At free-electron lasers, the beam intensity is so high that the sample is most probably destroyed by a single pulse. Therefore, the experiments with solid targets are organized so that new samples are supplied into each laser pulse. A specially prepared chip with samples is fixed to a mechanical device in a vacuum chamber. As a solid base for chips, silicon membranes or carbon films are usually used. During the experiment, the chip is shifted perpendicularly to the laser pulse according to the raster scheme so that each chip compartment is hit by a new pulse only once. The requirement to conduct an experiment in a vacuum chamber is dictated by the need to reduce the noise in the diffraction signal caused by scattering on air molecules. The chip itself is designed differently depending on the form in

which the samples are submitted. The following options for delivering samples on solid targets are used:

- Submission of samples in solution. This option is used to preserve living specimens (for example, cells) during the experiment in an environment similar to that in which they are in nature. A thin layer of samples surrounded by a thin layer of a solvent is placed between two layers of the Si<sub>3</sub>N<sub>4</sub> membrane in the compartments of a special chip that form a lattice. On SACLA, a mechanical apparatus for delivering samples on solid targets is created [100]. The chip is mounted on this device in a vacuum chamber. During the experiment, it is shifted perpendicularly to the laser pulse according to the raster scheme so that each chip compartment intersects with a new laser pulse only once. This method of sample delivery was used to collect data on SACLA for cells from *Microbacterium lacticum* [58].

- Delivery of samples in dried form. This method was used in experiments with human chromosomes [101]. A chromosome solution was placed on a special membrane, washed, and, then, the chromosomes were dried either in the open air or using chemical reagents. Experiments with dried samples of non-crystalline amyloid fibrils were similarly organized on LCLS; the samples were delivered in a pulse on a graphene substrate [102].

- Delivery of frozen samples at cryogenic temperatures on a solid target. This method is used to investigate the structure of fixed frozen undisturbed samples. In this delivery option, a similar raster mechanical setup in a vacuum chamber is used. However, it is not a chip with special compartments containing a liquid solution of samples, which is fixed on the apparatus, but a membrane with frozen samples prepared by a special fast freezing procedure. The membrane is attached to a metal disk with windows. During the experiment, the sample disk is shifted each time in increments of 25–50 μm to ensure that new fresh samples enter into the pulse. This method of sample delivery was used, for example, on SACLA in a series of experiments with samples of chloroplasts from *C. melorae* and cells from *E. coli* [103].

## 4.2. Detectors

The development of free-electron lasers possessing a high pulse frequency (for example, up to 4.5 MHz on EuXFEL) and a high intensity of each pulse (e.g., each pulse on EuXFEL contains up to 10<sup>12</sup> photons [104]) also required the creation of new detectors with a wide sensitivity range from one photon to 10<sup>4</sup> photons and higher per pulse per pixel, and a high speed of writing and reading the data. The sensitivity of the detector to individual photons is particularly important for experiments with single particles, in which the diffraction intensity can be of several photons per diffraction pattern [105].

A detector that meets these requirements is, for instance, the Adaptive Gain Integrating Pixel Detector (AGIPD) [106–108] developed in 2017 and installed on the SPB/SFX station EuXFEL. Note that this is not the only detector used on EuXFEL and other free electron lasers. PnCCD, CSPAD [109] and ePIX [110] are used on LCLS, MPCCD is used on SACLA, and the adJUstiNg Gain detector FoR the Aramis User station (JUNGFRAU) is used on SwissFEL [111, 112]. The AGIPD detector is a hybrid detector, which means that the photodiode and microelectronics belong to different blocks and can be improved independently of each other. The detector has four identical parts, each of which can move independently of the others and consists of four panels. Each panel is a monolithic silicon sensor and is a separate device. By a shift of the detector parts relative to each other, one can create a horizontal gap between the parts and a space in the center for the central part of the beam to pass through the detector. The total number of pixels (independent recording elements) is 1024·1024, i.e., approximately one million. The size of a single pixel is 200·200 μm. Each pixel has analog memory and can store up to 352 images. A detailed description of the sensor part of each panel and electronic equipment can be found in [108, 113]. Images are stored in the detector's memory during a single pulse bunch (“train”) and read during the interval between the bunches, which on EuXFEL lasts 99.4 milliseconds. The

detector has a low noise level, which allows the detection of weak signals from a few photons [108]. The detector is installed on a special platform. The vacuum chamber where the X-ray pulse intersects with the sample, as well as all devices located further along the X-ray beam, including the detector, are mounted on a common rail system, which allows one to move the equipment along it. In particular, this makes it possible to move the platform with the detector to change the distance between the area of intersection of the pulse with the sample and the detector at EuXFEL from 120 mm to 6 m [114].

### 4.3. Data storage

An X-ray free electron laser generates pulses in batches (or “trains”). On EuXFEL, a single batch consists of up to 2700 pulses. Ten batches are generated per second. Each pulse produces a single raw diffraction pattern, which contains readings from all the detector pixels. Thus, during EuXFEL experiment in which 1-megapixel detector is used, the amount of data recorded per laser pulse is 2 Mbytes, and the amount of data can be up to 10 Gbytes per second [115]. Note that LCLS-II, which is currently under construction, will emit up to 1 million pulses per second. Such a huge amount of raw data, as well as the necessary calibration parameters, required the creation of special systems for monitoring, processing, and storage of data on each laser. For example, on EuXFEL, during the experiment, the main parameters are monitored and continuously displayed using the system Karabo [116], which also later provides the user with the calibrated data [117]. All raw data are stored for users for later analysis on the Maxwell cluster. The user, in turn, has to know the specification of HDF5 format in which the data are stored, and to work with libraries that operate on files in this format (e.g., with the Python libraries pandas and xarray), as well as with modern tools for interactive work with data, such as Jupyter Notebooks.

### 4.4. Data processing

After the diffraction experiment finished, i.e., a large number of diffraction patterns have been collected, the following main stages of data analysis and processing are performed:

- Estimation of noise in order to subtract it from the useful signal. This stage is not always the first one. It is often done after the 2nd or the 3rd stages.
  - Selection of diffraction patterns containing a useful signal and their classification. Selection and classification are carried out in different order, sometimes in several stages [118].
  - Determination of the mutual orientation of two-dimensional diffraction patterns. Calculation of three-dimensional diffraction intensity function  $I(\mathbf{s}) = |\mathbf{F}(\mathbf{s})|^2$ .
- Let us consider in detail each of the stages and the problems that arise.

In the experiment, a huge set of images (“frames”) is collected. However, not all of them can be used at the next stages of the structure determination. In the vast majority of cases, an X-ray pulse does not intersect with the sample, and, accordingly, the resulting frames are empty, i.e. they contain only background noise, the main contribution to which is made by the background from the injector and from the scattering on gas molecules in the vacuum tube. These frames have to be sorted out. Later, they can be used, along with “dark runs”, to estimate the noise that must be subtracted from the frames containing a useful signal. The procedure for selecting non-empty frames containing a scattering signal is called hit finding. It can be performed using the programs Redflamingo, Hummingbird [119], Cheetah [120], CASS [121, 122], and Psana [123]. We emphasize that the problem of the recognition of a useful signal and the subtraction of noise is not at all trivial. First, the intensity of the useful signal in many cases is very small. Second, the experimental noise does not follow the Gaussian distribution and changes from frame to frame, which complicates the separation of photons scattered by the particle and “noise” photons, and, ultimately, greatly complicates the solution of the structure (to the point that makes the solution impossible).

After non-empty frames have been selected, the task of their further classification arises. Among non-empty frames, there are those obtained from the intersection of the beam with a single particle, with more than one individual particles, with complexes of several clumped particles, with clusters of gas molecules or water droplets. To determine the orientation of a single particle, it is necessary to select from all the diffraction patterns only those that correspond to the diffraction from one single particle. Different approaches have been tried to solve this problem. Rose and co-authors [118] compared the results of application of two different approaches to the selection of frames corresponding to the single particle from the same experimental set of non-empty frames. The first approach involved the diffusion map method [124, 125], and the second one used a multi-stage frame selection procedure in combination with the principal component method. The data were collected at LCLS in experiments with single particles of the bacteriophage PR772. Using the diffusion map method, 14772 frames were selected from 44039 non-empty frames [90]. In the second approach, the authors decided to use not all 44039 frames, but only sufficiently strong ones. The initial 44039 frames were first sorted according to the value of the integral intensity, and, for further analysis, the data selected at different cut levels were compared. The need to select different levels was dictated by the fact that, on the one hand, the authors wanted to select as many frames with a strong signal as possible, and, on the other hand, among the frames with a strong signal there were frames with scattering from several particles. It is desirable that the relative number of these frames be small. The authors performed further procedures for three different cut-off levels. Before the method of principal components has been applied, a data compression was performed. In a recent paper [127], it was shown that the blurring (weakness) of the signal is not a problem in itself. Apparently, the main problem is still the presence of changing noise.

In [128], the authors modified the experimental data collected earlier at LCLS. They tried to simulate either diffraction from a smaller particle or a weaker experimental diffraction intensity. The weakening of experimental data was simulated in two variants: a decrease in the number of photons and a decrease in the number of diffraction patterns. Instead of initial 14772 diffraction patterns, the authors randomly selected 8192, 4096, 20148, 1024, and 512. It was shown that, even when the original experimental data were weakened, it was possible to determine the structure of the object.

For the serial scheme of the delivery of the particles into the beam, a significant problem during the data processing is that the particles fall into the X-ray beam in arbitrary, previously unknown orientations. "Post-experimental" determination of the mutual orientation of exposed particles is necessary to correctly index the diffraction patterns, i.e., for each point of a two-dimensional diffraction pattern, to determine the corresponding three-dimensional scattering vector (3). A few approaches have been proposed to solve this problem.

The most well-known approach to the determination of the orientation of a single particle is the common arc method, which is based on the same idea as the common lines method used in electron microscopy. The idea is as follows. All the scattering vectors corresponding to the pixels of the detector matrix lie on a spherical surface of radius  $1/\lambda$  that passes through the origin of the inverse space coordinates (Fig. 2). When the object is rotated, this spherical surface rotates. The surfaces that correspond to two different orientations of the object have a common intersection line to which the curves with the same intensity values on the two diffraction patterns correspond. Having found the curves that coincide in intensity on two X-ray images it becomes possible to determine the mutual orientation of particles at the moment of exposure. However, the use of this approach is difficult in the case of complex objects in an experiment with a high noise level.

Among the algorithms that are being developed to solve this problem, the so-called Expand-Maximize-Compress (EMC) algorithm [129], implemented in the Dragonfly program [130], is currently the most advanced. We emphasize that this algorithm was applied not only to model data, but also to real experimental diffraction data collected at LCLS. It was

successfully applied for the first time to solve the structure of mimivirus [89] and, then, the structures of the bacteriophage PR772 [118] and Melbourne virus [92]. The algorithm is an iterative procedure. At each step of this procedure, a set of diffraction patterns corresponding to different orientations of a trial model is calculated (Expansion step). Then, for each of the experimental and calculated diffraction patterns, a function is calculated that quantitatively characterizes their “degree of similarity” (Maximization step). A new trial model is assembled from the experimental diffraction patterns (Compress step). In this case, the diffraction patterns calculated at the previous step are not directly replaced by the experimental diffraction patterns, but each new “trial” diffraction pattern is the sum of all diffraction patterns with the weights determined at the previous step of Maximization.

To plan an experiment with single particles at X-ray lasers numerical simulation programs can be useful. The user can apply, for example, S2Esim [131] software packages created at EuXFEL and Condor [132] created at the Uppsala University (Sweden).

## 5. THREE-DIMENSIONAL RECONSTRUCTION OF ISOLATED PARTICLES FROM X-RAY SCATTERING DATA

### 5.1. Virtual crystal

Theoretically, an X-ray diffraction experiment with an isolated particle allows one to determine the intensity of scattered waves  $I(\mathbf{s}) = |\mathbf{F}(\mathbf{s})|^2$  for all scattering vectors  $\mathbf{s}$  that satisfy the condition  $|\mathbf{s}| \leq d_{\text{lim}}^{-1}$ , with  $d_{\text{lim}} = \lambda/2$ , where  $\lambda$  is the wavelength of X-rays. The analytical properties of the Fourier transform of a function with a finite support theoretically allow one to extrapolate these values to all vectors of the reciprocal space  $\mathbf{s} \in \mathbf{R}^3$ , but, today, there is no practical algorithm to perform this extrapolation [1, 133]. In practice, the result of the experiment is a discrete set of diffraction patterns corresponding to different orientations of the object relative to the primary beam. Each of these diffraction patterns contains information for a discrete set of pixels of the detector matrix. The scattering vectors  $\mathbf{s}$  corresponding to the pixels of a particular X-ray image are located on the surface of one of the spheres (of radius  $1/\lambda$ ) in the reciprocal space that passes through the origin. The discretization of the experimental data set consists in extrapolation of the measured values to the regular lattice  $\mathcal{R}' = \{\mathbf{s}_{hkl}\}$  in the reciprocal space:

$$\mathbf{s}_{hkl} = h\mathbf{a}^* + k\mathbf{b}^* + l\mathbf{c}^*, \quad h, k, l - \text{integer} . \quad (11)$$

Here  $\mathbf{a}^*, \mathbf{b}^*, \mathbf{c}^*$  are selected vectors that define the basis of the lattice. In the case of a crystal object, the choice of basis  $\mathbf{a}^*, \mathbf{b}^*, \mathbf{c}^*$  is predetermined. These are vectors conjugated to the vectors  $\mathbf{a}, \mathbf{b}, \mathbf{c}$  that define the unit cell of the crystal. The lattice nodes  $\mathcal{R}'$ , in this case, are Bragg reflections, i.e. those reflections for which the experiment allows one to measure the intensities, and which are necessary to calculate the electron density in the form of the Fourier series (9). When the object is an isolated particle, the vectors  $\mathbf{a}^*, \mathbf{b}^*, \mathbf{c}^*$  can be chosen rather arbitrarily [1, 133]. As a rule, they are chosen orthogonal and of equal length. A parallelepiped  $V$  constructed on its conjugate vectors  $\mathbf{a}, \mathbf{b}, \mathbf{c}$  can be called a virtual crystal cell. The Fourier series (9) calculated from a set of reflections  $\mathcal{R}'$  is a periodic function each unit cell of which contains the image of a single particle surrounded by a region with zero electron density (the "solvent region"). The choice of the periods  $\mathbf{a}, \mathbf{b}, \mathbf{c}$  of the virtual crystal that exceed the object dimensions, or, what is the same, the choice of sufficiently small sampling steps, allows one to formulate the problem of the structure determination as a common problem of X-ray diffraction analysis. This analysis is based on the knowledge of set of magnitudes of structure factors for a (virtual) crystal structure, to reconstruct the electron density distribution in it [1].

## 5.2. Projection methods for reconstruction of electron density

Freedom of choice of the size of the unit cell of a virtual crystal in studies of isolated particles allows you to deal with the cells a significant part of which is occupied by a solvent. This situation is particularly favorable for using the methods of "electron density modification" proposed in the 70s of the 20th century [134–138], in particular, "solvent flattening" [134, 139, 140]. When using the latter method, it is assumed that the unit cell is divided into the region of the molecule and the region of the solvent. In general, the method consists of a cyclic application of two steps:

- A. Solvent smoothing. The electron density distribution calculated in some way is modified: its values in the area occupied by the solvent are forcibly set to 0.
- B. Substitution of magnitudes. According to the modified density distribution, the structure factors are calculated  $F^{calc}(\mathbf{s})\exp i\varphi^{calc}(\mathbf{s})$  using formula (8). The phases of the calculated structure factors are used together with the experimental values of the magnitudes  $F^{obs}(\mathbf{s})$  to calculate the new density distribution by formula (9).

From the mathematical point of view, the operation of zeroing the density in the solvent region and the procedure of the substitution of the magnitudes in Fourier synthesis can be called "projectors". The purpose of the procedure is to find an electron density distribution that simultaneously has the correct (experimental) values of the structure factor magnitudes and is equal (or close to) to zero in the solvent region.

The convergence rate of the iterative procedure can be increased by using so-called "reflectors". For the projector  $P$ , the reflector  $R$  is defined by the equality  $R = 2P - I$ , where  $I$  is the identity operator. The reflector reinforces the tendency of the change of the object, introduced by the projector. Thus, if the action of the projector of "density zeroing" in the solvent region is to replace the value  $\rho$  by 0, then the action of the reflector is to replace it by  $-\rho$ . The action of the reflector corresponding to the operation of the magnitude substitution is to calculate the Fourier synthesis (9) with the coefficients  $(2F^{obs}(\mathbf{s}) - F^{calc}(\mathbf{s}))\exp i\varphi^{calc}(\mathbf{s})$ . The use of reflectors can significantly speed up the convergence, but it can make, as well, the procedure less stable. Therefore, numerous approaches based on different alternation of these two pairs of projectors and reflectors have been proposed [135, 139, 141–145]. All the examples described in section 6 of the determination of the structures of isolated particles were obtained using various modifications of these methods.

## 5.3. Connected masks of a molecule region as a tool for solving the phase problem

The methods described above, which use solvent smoothing imply that the mask of the molecule region is known, i.e., it is indicated which points of the virtual unit cell belong to the region of the molecule and which do not. At the initial stage of the study, this information is not available, and incorrect assignment of the area of the molecule can lead to incorrect results. Several approaches to the determination (refinement) of the boundaries of the molecular region based on filtering highly noisy Fourier syntheses have been proposed [140, 146–148]. It should also be noted that iterative procedures may turn out to be divergent, converge to false solutions, or get stuck at some critical points. The procedure based on a random search for a connected mask of a molecule [149–153] can serve as a preliminary iterative stage for solving the phase problem. The approach is based on a randomly generation of a large number (millions) of hypothetical connected masks of the molecule region. The generated mask is considered acceptable if the magnitudes of structure factors calculated from it accurately reproduce their experimental values. Acceptable masks are stored for further use. The generation process continues until the specified number (for example, 100) of admissible masks is reached. The sets of structure factors corresponding to the selected masks are aligned

and averaged. The found phase values can be used for calculating the Fourier synthesis or as input data for programs that refine the phase values.

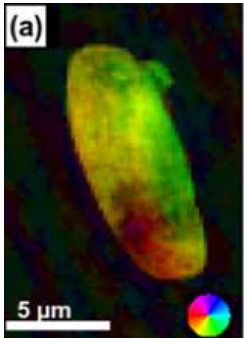
## 6. DETERMINATION OF THE STRUCTURE OF ISOLATED PARTICLES. EXAMPLES

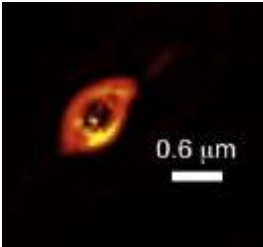
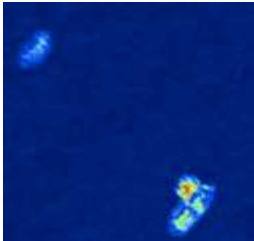
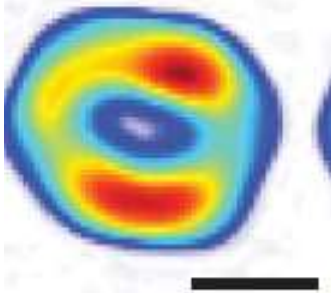
During the past decade, a number of experiments have been conducted at free-electron lasers, in which diffraction from single biological particles has been obtained [11, 58, 86, 88–90, 92, 118, 154–158]. The performance of these experiments involves overcoming numerous experimental difficulties and is itself a great achievement in biological crystallography.

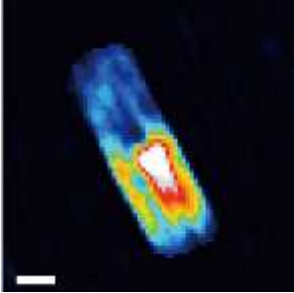
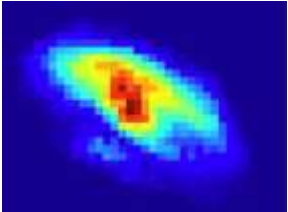
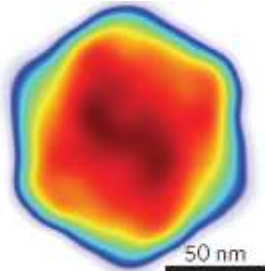
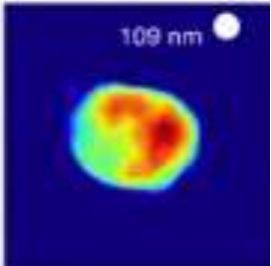
In numerical experiments with simulated data, it was shown that with modern parameters of free-electron lasers, the solution of structures of isolated particles is a feasible task [159]. Besides, there are experimental works carried out on synchrotrons in which the geometry of the experiment was the same as in free-electron lasers, and it was demonstrated that, even despite the weak and smeared signal on the detector, the reconstruction of a three-dimensional object is quite possible [127]. However, in a real experiment with single biological particles, a number of factors appear that greatly complicate this task. These factors include, first of all, the inhomogeneity of the particles that fall into the beam (all particles are not exactly of the same size, there may also be the presence of impurities, the formation of complexes of the particles under study with impurities, as well as the formation of complexes of particles with each other), and the presence of noise that cannot be properly modeled and that may change during the experiment.

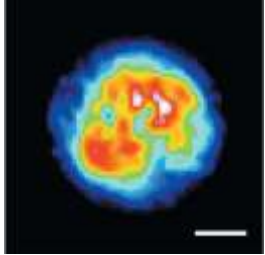
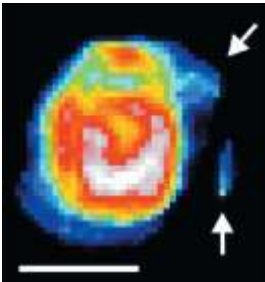
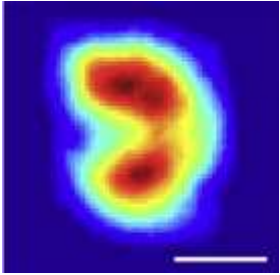
To date, only a small number of individual particles have been reconstructed, and only for a few of them the reconstruction is three-dimensional (see Tab. 1). Admittedly, these results do not yet look like sufficient evidence that the method for the determination of the three-dimensional structure of a single particle has been developed. The resolution obtained is very low. As a result, the final reconstructions give a fairly rough idea of the shape of the object and the reconstructed particles are similar to each other.

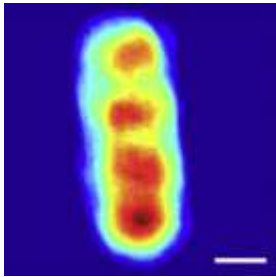
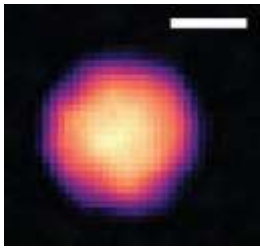
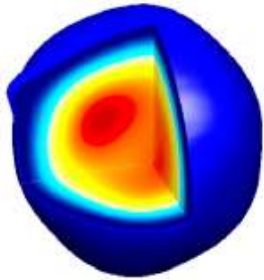
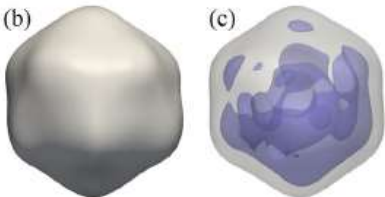
**Table 1.** Isolated (non-crystallized) biological objects whose structure was determined from experimental data collected on free-electron lasers

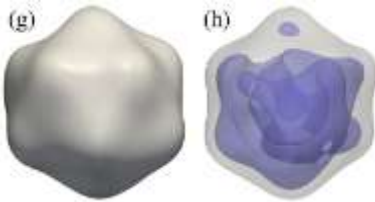
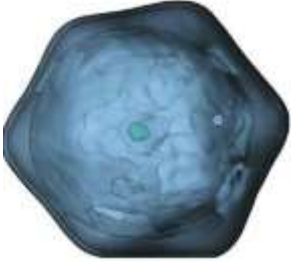
<b>Biological object.</b> <b>The place of the data collection, wavelength.</b> <b>The way of delivery of the object into the pulse.</b> <b>Reference.</b> <b>Code in the bank CXIDB [160].</b>	<b>Size of the object.</b> <b>The image of the object reconstructed by the authors.</b> <b>The estimation of the resolution calculated by the authors</b>	<b>Comments</b>
Cells from diatom <i>Navicula perminuta</i> . FLASH, 8 nm. Si <sub>3</sub> N <sub>4</sub> membrane. [154]	 <p>Resolution 380 nm.                      (The figure is reproduced from [154].)</p>	Resolution is limited by the size of the detector. Two-dimensional reconstruction. Projection methods [143].

<p><b>Biological object.</b>  <b>The place of the data collection, wavelength.</b>  <b>The way of delivery of the object into the pulse.</b>  <b>Reference.</b>  <b>Code in the bank CXIDB [160].</b></p>	<p><b>Size of the object.</b>  <b>The image of the object reconstructed by the authors.</b>  <b>The estimation of the resolution calculated by the authors</b></p>	<p><b>Comments</b></p>
<p>Cells from bacteria  <i>Spiroplasma melliferum</i>,  <i>Prochlorococcus marinus</i>,  <i>Synechococcus elongates</i>.                      FLASH, 13.5 nm.                      Si<sub>3</sub>N<sub>4</sub> membrane.                      [155]</p>	<p><i>S. melliferum</i>, size 5 μm × 0.15 μm.</p>  <p>Resolution 31 nm.</p> <p><i>P. marinus</i>, size 0.5 μm.</p>  <p>Resolution 83 nm</p> <p><i>S. elongatus</i>, size 1.5 μm × 0.8 μm</p>  <p>Resolution 38 nm.                      (The figures are reproduced from [155])</p>	<p>Two-dimensional reconstruction.                      Projection methods [143].</p>
<p><i>Acanthamoeba polyphaga</i>                      mimivirus.                      LCLS, 6.9 Å.                      Aerosol.                      [86].                      CXIDB ID 1</p>	<p>Size of the particle 450 nm.</p>  <p>200 nm</p> <p>Resolution 32 nm.                      (The figure is reproduced from [155])</p>	<p>Two-dimensional reconstruction.                      Projection methods [143].</p>

<p><b>Biological object.</b>  <b>The place of the data collection, wavelength.</b>  <b>The way of delivery of the object into the pulse.</b>  <b>Reference.</b>  <b>Code in the bank CXIDB [160].</b></p>	<p><b>Size of the object.</b>  <b>The image of the object reconstructed by the authors.</b>  <b>The estimation of the resolution calculated by the authors</b></p>	<p><b>Comments</b></p>
<p>Cells from <i>Microbacterium lacticum</i>.                      SACLA, 2.25 Å.                      Micro-liquid enclosure array.                      [58]</p>	<p>Size of the particle 194<sub>HM</sub> × 570<sub>HM</sub>.</p>  <p>Resolution 37<sub>HM</sub>.                      (The figure is reproduced from [58].)</p>	<p>Two-dimensional reconstruction.                      Projection methods [143]</p>
<p>RNAi microsponges                      SACLA, 2.48 Å.                      Si<sub>3</sub>N<sub>4</sub> membrane windows.                      [156]</p>	<p>Size of the particle 650<sub>HM</sub> × 820<sub>HM</sub>.</p>  <p>Resolution 70<sub>HM</sub>.                      (The figure is reproduced from [156].)</p>	<p>Two-dimensional reconstruction.                      Projection methods [143]</p>
<p>Carboxysomes from <i>Halothiobacillus neapolitanus</i>.                      LCLS.                      Aerosol.                      [87].                      CXIDB ID 25</p>	<p>Size of the particle 115<sub>nm</sub>.</p>  <p>Resolution 18.1<sub>HM</sub>.                      (The figure is reproduced from [87].)</p>	<p>Three-dimensional reconstruction.                      Projection methods [143]</p>
<p>Cells of cyanobacterium  <i>Cyanobium gracile</i>,  <i>Synechococcus elongates</i>.                      LCLS.                      Aerosol.                      [88].                      CXIDB ID 26</p>	<p>Size of the cell                      0.25–0.4 μm * 0.4–4.0 μm.</p>  <p>Resolution 109<sub>nm</sub>.                      (The figure is reproduced from [88].)</p>	<p>Two-dimensional reconstruction.                      Projection methods [143]</p>

<p><b>Biological object.</b>  <b>The place of the data collection, wavelength.</b>  <b>The way of delivery of the object into the pulse.</b>  <b>Reference.</b>  <b>Code in the bank CXIDB [160].</b></p>	<p><b>Size of the object.</b>  <b>The image of the object reconstructed by the authors.</b>  <b>The estimation of the resolution calculated by the authors</b></p>	<p><b>Comments</b></p>
<p><i>Acanthamoeba polyphaga</i> mimivirus.                      LCLS.                      Aerosol.                      [89].                      CXIDB ID 30</p>	<p>Size of the particle 450 nm.</p>  <p>Resolution 125 nm.                      (The figure is reproduced from [89] with the permission of ©American Physical Society, 2015)</p>	<p>Three-dimensional reconstruction.                      Projection methods [143].</p>
<p>Chloroplasts from red algae <i>Cyanidioschyzon merolae</i>.                      Minicells from <i>E. coli</i> strain ME8077.                      SACLA.                      Carbon and silicon nitride membrane .                      [103]</p>	<p>Chloroplast, the size 1.7 <math>\mu\text{m}</math>.</p>  <p>500<sub>HM</sub></p> <p>Minicell, the size 800 <sub>HM</sub>.</p>  <p>500 nm</p> <p>Resolution 52 nm.                      (The figures are reproduced from [103].)</p>	<p>Two-dimensional reconstruction.                      Projection methods [143]</p>
<p>Cells of bacteria <i>Staphylococcus aureus</i>.                      SACLA.                      Si<sub>3</sub>N<sub>4</sub> membrane.                      [161]</p>	<p>Two connected daughter cells.</p>  <p>300 nm</p> <p>Resolution 143.5 nm.</p>	<p>Two-dimensional reconstruction.                      Projection methods [143]</p>

<p><b>Biological object.</b>  <b>The place of the data collection, wavelength.</b>  <b>The way of delivery of the object into the pulse.</b>  <b>Reference.</b>  <b>Code in the bank CXIDB [160].</b></p>	<p><b>Size of the object.</b>  <b>The image of the object reconstructed by the authors.</b>  <b>The estimation of the resolution calculated by the authors</b></p>	<p><b>Comments</b></p>
	<p>Four connected daughter cells.</p>  <p>300<sub>HM</sub></p> <p>Resolution 54 nm.                      (The figures are reproduced from [161].)</p>	
<p>Omono river virus.                      LCLS.                      Aerosol.                      [91].                      CXIDB ID 56</p>	<p>Size of the particles 35 – 300 nm.</p> <p>20 nm</p>  <p>Resolution 13.5 nm.                      (The figure is reproduced from [91].)</p>	<p>Two-dimensional reconstruction.                      Projection methods [143].</p>
<p>Bacteriophage PR772.                      LCLS.                      Aerosol.                      [162].                      Data collection [90].                      CXIDB ID 58</p>	<p>Size of the particle 70 nm.</p>  <p>Resolution 9 nm.                      (The figure is reproduced from [90].)</p>	<p>Three-dimensional reconstruction.                      Projection methods [143]</p>
<p>Rice Dwarf Virus.                      LCLS.                      Aerosol.                      [78].                      Data collection [77].                      CXIDB ID 36</p>	<p>Size 69–72 nm.</p>  <p>Resolution 17.7 nm.                      (The figures are reproduced from [78].)</p>	<p>Three-dimensional reconstruction.                      Projection methods [143]</p>

<b>Biological object.</b> <b>The place of the data collection, wavelength.</b> <b>The way of delivery of the object into the pulse.</b> <b>Reference.</b> <b>Code in the bank CXIDB [160].</b>	<b>Size of the object.</b> <b>The image of the object reconstructed by the authors.</b> <b>The estimation of the resolution calculated by the authors</b>	<b>Comments</b>
Bacteriophage PR772. LCLS. [78]. Data collection [90]	Size of the particle 67.5–70.5 nm.  Resolution 17.7 nm. (The figures are reproduced from [78].)	Three-dimensional reconstruction. Projection methods [143].
Bacteriophage PR772. LCLS. [118]. Data collection [90]	Size of the particle 68.5 nm.  Resolution 9 nm. (The figure is reproduced from [118].)	Three-dimensional reconstruction. Projection methods [143].
Melbourne virus (MeIV). LCLS. Aerosol. [92]	Size of the particle 230 nm.  Resolution 28 nm. (The figure is reproduced from [92].)	Three-dimensional reconstruction. Projection methods [143].

## 7. CONCLUSIONS

In recent years, the approach of open scientific research and the creation of large scientific consortia that bring together specialists in various fields have become increasingly popular in many fields, including X-ray diffraction from a single particle. In the fall of 2014, at a conference at SLAC, more than 100 scientists announced the creation of an international consortium known as the Single Particle Imaging Initiative (SPI). A program was approved, the so-called “road map” [163]. The goal was to determine the structure of isolated biological particles at atomic resolution. Two years later, the consortium members published data collected for the rice mosaic virus with a resolution of up to 5.9 Å [77]. (The best resolution

for solved non-crystalline biological structures is currently estimated at 9 nm [162]). The data for the rice mosaic virus experiment, as well as for a number of other diffraction experiments with isolated biological particles, are publicly available in the Coherent X-ray Imaging Data Bank CXIDB [160]. There are also processing protocols for many experiments. The source codes of programs can be downloaded from Github, and one can also participate in their creation, i.e. the texts of software packages are created by researchers from different groups. Since the beginning of the European laser, this style of work, in large scientific associations, continues in this area [134]. The efforts of scientists from many countries are aimed at the improvement the methodology of the experiment at all its stages and solution of many of the fundamental problems described in this review.

The research was carried out with the financial support of the RFBR in the framework of research project No. 19-14-50165. The authors are grateful to N. L. Lunina for her assistance in preparing the manuscript.

## REFERENCES

1. Lunin V.Y., Lunina N.L., Petrova T.E. Single Particle Study by X-Ray Diffraction: Crystallographic Approach. *Math. Biol. Bioinf.*. 2019. V. 14. №2. P. 500–516. doi: [10.17537/2019.14.500](https://doi.org/10.17537/2019.14.500)
2. Landau L.D., Lifshitz E.M. *Mechanics*, 3d edition. Butterworth-Heinemann; 1976. 224 p.
3. Landau L.D., Lifshitz E.M. *The Classical Theory of Fields*, 4th edition. Butterworth-Heinemann; 1980. 402 p.
4. Urzhumtsev A.G., Lunin V.Y. Introduction to crystallographic refinement of macromolecular atomic models. *Crystallography Reviews*. 2019. V. 25. P. 164–262. doi: [10.1080/0889311X.2019.1631817](https://doi.org/10.1080/0889311X.2019.1631817)
5. Blundell T.L., Johnson L.N. *Protein Crystallography*. Academic Press, 1976. 620 p.
6. Serdyuk I.N., Zaccalai N.R., Zaccalai J. *Methods in Molecular Biophysics: Structure, Dynamics, Function*. 2-nd edition. Cambridge University Press, 2017. 702 p.
7. Rupp B. *Biomolecular Crystallography: Principles, Practice, and Applications to Structural Biology*. New York: Garland Science, Taylor and Francis Group, 2010. P. xxi + 809.
8. Urzhumtseva L., Klahlolz B., Urzhumtsev A. On effective and optical resolutions of diffraction data sets. *Acta Crystallographica D*. 2013. V. 69. P. 1921–1934. doi: [10.1107/S0907444913016673](https://doi.org/10.1107/S0907444913016673)
9. Van Heel M., Schatz M. Fourier shell correlation threshold criteria. *J. Struct. Biol.* 2005. V. 151. P. 250–262. doi: [10.1016/j.jsb.2005.05.009](https://doi.org/10.1016/j.jsb.2005.05.009)
10. Van Heel M., Schatz M. Reassessing the Revolution's Resolutions. *bioRxiv*. 2017. Article No. 224402. doi: [10.1101/224402](https://doi.org/10.1101/224402)
11. Sobolev E., Zolotarev S., Giewekemeyer K., Bielecki J., Okamoto K., Reddy H.K.N, Andreasson J., Ayyer K., Barak I., Bari S. et al. Megahertz single-particle imaging at the European XFEL. *Communications Physics*. 2020. V. 3. Article No. 97. doi: [10.1038/s42005-020-0362-y](https://doi.org/10.1038/s42005-020-0362-y)
12. Georgescu I. The first decade of XFELs. *Nature Reviews Physics*. 2020. V. 2. Article No. 345. doi: [10.1038/s42254-020-0204-6](https://doi.org/10.1038/s42254-020-0204-6)
13. Margaritondo G., Ribič P.R. A simplified description of X-ray free-electron lasers. *J. Synchrotron Radiation*. 2011. V. 18. P. 101–108. doi: [10.1107/S090904951004896X](https://doi.org/10.1107/S090904951004896X)
14. Pellegrini C. The history of X-ray free-electron lasers. *Eur. Phys. J. H*. 2012. V. 37. P. 659–708. doi: [10.1140/epjh/e2012-20064-5](https://doi.org/10.1140/epjh/e2012-20064-5)

15. White T.A., Mariani V., Brehm W., Yefanov O., Barty A., Beyerlein K.R., Chervinskii F., Galli L., Gati C., Nakane T. et al. Recent developments in CrystFEL. *J. Appl. Cryst.* 2016. V. 49. P. 680–689. doi: [10.1107/S1600576716004751](https://doi.org/10.1107/S1600576716004751)
16. Chapman H.N., Fromme P., Barty A., White T.A., Kirian R.A., Aquila A., Hunter M.S., Schulz J., DePonte D.P., Weierstall U. et al. Femtosecond X-ray protein nanocrystallography. *Nature*. 2011. V. 470. P. 73–77. doi: [10.1038/nature09750](https://doi.org/10.1038/nature09750)
17. Boutet S., Lomb L., Williams G.J., Barends T.R., Aquila A., Doak R.B., Weierstall U., DePonte D.P., Steinbrener J., Shoeman R.L. et al. High-resolution protein structure determination by serial femtosecond crystallography. *Science*. 2012. V. 337. P. 362–364. doi: [10.1126/science.1217737](https://doi.org/10.1126/science.1217737)
18. Kern J., Alonso-Mori R., Hellmich J., Tran R., Hattne J., Laksmono H., Glöckner C., Echols N., Sierra R.G., Sellberg J. et al. Room temperature femtosecond X-ray diffraction of photosystem II microcrystals. *Proc Natl Acad Sci USA*. 2012. V. 109. P. 9721–9726. doi: [10.1073/pnas.1204598109](https://doi.org/10.1073/pnas.1204598109)
19. Kupitz C., Basu S., Grotjohann I., Fromme R., Zatsepin N.A., Rendek K.N., Hunter M.S., Shoeman R.L., White T.A., Wang D. et al. Serial time-resolved crystallography of photosystem II using a femtosecond X-ray laser. *Nature*. 2014. V. 513. P. 261–265. doi: [10.1038/nature13453](https://doi.org/10.1038/nature13453)
20. Sierra R.G., Gati C., Laksmono H., Dao E.H., Gul S., Fuller F., Kern J., Chatterjee R., Ibrahim M., Brewster A.S. et al. Concentric-flow electrokinetic injector enables serial crystallography of ribosome and photosystem II. *Nat. Methods*. 2016. V. 13. P. 59–62. doi: [10.1038/nmeth.3667](https://doi.org/10.1038/nmeth.3667)
21. Liu W., Wacker D., Gati C., Han G.W., James D., Wang D., Nelson G., Weierstall U., Katritch V., Barty A. et al. Serial femtosecond crystallography of G protein-coupled receptors. *Science*. 2013. V. 342. P. 1521–1524. doi: [10.1126/science.1244142](https://doi.org/10.1126/science.1244142)
22. Kang Y., Zhou X.E., Gao X., He Y., Liu W., Ishchenko A., Barty A., White T.A., Yefanov O., Han G.W. et al. Crystal structure of rhodopsin bound to arrestin by femtosecond X-ray laser. *Nature*. 2015. V. 523. P. 561–567. doi: [10.1038/nature14656](https://doi.org/10.1038/nature14656)
23. Johansson L.C., Arnlund D., White T.A., Katona G., DePonte D.P., Weierstall U., Doak R.B., Shoeman R.L., Lomb L., Malmerberg E. et al. Lipidic phase membrane protein serial femtosecond crystallography. *Nat Methods*. 2012. V. 9. P. 263–265. doi: [10.1038/nmeth.1867](https://doi.org/10.1038/nmeth.1867)
24. Johansson L.C., Arnlund D., Katona G., White T.A., Barty A., DePonte D.P., Shoeman R.L., Cecilia Wickstrand C., Sharma A., Williams G.J. et al. Structure of a photosynthetic reaction centre determined by serial femtosecond crystallography. *Nat. Commun.* 2013. V. 4. Article No. 2911. doi: [10.1038/ncomms3911](https://doi.org/10.1038/ncomms3911)
25. Weierstall U., James D., Wang C., White T.A., Wang D., Liu W., Spence J.C.H., Doak R.B., Nelson G., Fromme P. et al. Lipidic cubic phase injector facilitates membrane protein serial femtosecond crystallography. *Nat. Commun.* 2014. V. 5 Article No. 3309. doi: [10.1038/ncomms4309](https://doi.org/10.1038/ncomms4309)
26. Gati C., Oberthür D., Yefanov O., Bunker R.D., Stellato F., Chiu E., Yeh S.M., Aquila A., Basu S., Bean R. et al. Atomic structure of granulins determined from native nanocrystalline granulovirus using an X-ray free-electron laser. *Proc. Natl. Acad. Sci. USA*. 2017. V. 114. P. 2247–2252. doi: [10.1073/pnas.1609243114](https://doi.org/10.1073/pnas.1609243114)
27. Grünbein M.L., Bielecki J., Gorel A., Stricker M., Bean R., Cammarata M., Dörner K., Fröhlich L., Hartmann E., Hauf S. et al. Megahertz data collection from protein microcrystals at an X-ray free-electron laser. *Nat. Commun.* 2018. V. 9. Article No. 3487. doi: [10.1038/s41467-018-05953-4](https://doi.org/10.1038/s41467-018-05953-4)
28. Wiedorn M.O., Oberthür D., Bean R., Schubert R., Werner N., Abbey B., Aepfelbacher M., Adriano L., Allahgholi A., Al-Qudami N. et al. Megahertz serial crystallography. *Nat. Commun.* 2018. V. 9. Article No. 4025. doi: [10.1038/s41467-018-06156-7](https://doi.org/10.1038/s41467-018-06156-7)

29. Gisriel C., Coe J., Letrun R., Yefanov O.M., Luna-Chavez C., Stander N.E., Lisova S., Mariani V., Kuhn M., Aplin S. et al. Membrane protein megahertz crystallography at the European XFEL. *Nat. Commun.* 2019. V. 10. Article No. 5021. doi: [10.1038/s41467-019-12955-3](https://doi.org/10.1038/s41467-019-12955-3)
30. Glowia J.M., Cryan J., Andreasson J., Belkacem A., Berrah N., Blaga C., Bostedt C., Bozek J., DiMauro L., Fang L. et al. Time-resolved pump-probe experiments at the LCLS. *Opt. Express.* 2010. V. 18. P. 17620–17630. doi: [10.1364/OE.18.017620](https://doi.org/10.1364/OE.18.017620)
31. Aquila A., Hunter M.S., Doak R.B., Kirian R.A., Fromme P., White T.A., Andreasson J., Arnlund D., Bajt S., Barends T.R.M. et al. Time-resolved protein nanocrystallography using an X-ray free-electron laser. *Opt. Express.* 2012. V. 20. P. 2706–2716. doi: [10.1364/OE.20.002706](https://doi.org/10.1364/OE.20.002706)
32. Tenboer J., Basu S., Nadia Zatsepin N., Pande K., Milathianaki D., Frank M., Hunter M., Boutet S., Williams G.J., Koglin J.E. et al. Time-resolved serial crystallography captures high-resolution intermediates of photoactive yellow protein. *Science.* 2014. V. 346. P. 1242–1246. doi: [10.1126/science.1259357](https://doi.org/10.1126/science.1259357)
33. Barends T.R., Foucar L., Ardevol A., Nass K., Aquila A., Botha S., Doak R.B., Falahati K., Hartmann E., Hilpert M. et al. Direct observation of ultrafast collective motions in CO myoglobin upon ligand dissociation. *Science.* 2015. V. 350. P. 445–450. doi: [10.1126/science.aac5492](https://doi.org/10.1126/science.aac5492)
34. Pande K., Hutchison C.D.M., Groenhof G., Aquila A., Robinson J.S., Tenboer J., Basu S., Boutet S., DePonte D.P., Liang M. et al. Femtosecond structural dynamics drives the trans/cis isomerization in photoactive yellow protein. *Science.* 2016. V. 352. P. 725–729. doi: [10.1126/science.aad5081](https://doi.org/10.1126/science.aad5081)
35. Kubo M., Nango E., Tono K., Kimura T., Owada S., Song C., Mafuné F., Miyajima K., Takeda Y., Kohno J.Y. et al. Nanosecond pump–probe device for time-resolved serial femtosecond crystallography developed at SACLA. *J. Synchrotron Radiat.* 2017. V. 24. P. 1086–1091. doi: [10.1107/S160057751701030X](https://doi.org/10.1107/S160057751701030X)
36. Pandey S., Bean R., Sato T., Poudyal I., Bielecki J., Villarreal J.C., Yefanov O., Mariani V., White T.A., Kupitz C. et al. Time-resolved serial femtosecond crystallography at the European XFEL. *Nat. Methods.* 2020. V. 17. P. 73–78. doi: [10.1126/science.aad5081](https://doi.org/10.1126/science.aad5081)
37. Lunin V.Y., Lunina N.L., Petrova T.E. The biological crystallography without crystals. *Mathematical Biology and Bioinformatics.* 2017. V. 12. P. 55–72. doi: [10.17537/2017.12.55](https://doi.org/10.17537/2017.12.55)
38. Neutze R., Wouts R., van der Spoel D., Weckert E., Hajdu J. Potential for biomolecular imaging with femtosecond X-ray pulses. *Nature.* 2000. V. 406. P. 752–757. doi: [10.1038/35021099](https://doi.org/10.1038/35021099)
39. Cryan J.P., Glowia J.M., Andreasson J., Belkacem A., Berrah N., Blaga C.I., Bostedt C., Bozek J., Buth C., DiMauro L.F. et al. Auger electron angular distribution of double core-hole states in the molecular reference frame. *Phys. Rev. Lett.* 2010. V. 105. Article No. 083004. doi: [10.1103/PhysRevLett.105.083004](https://doi.org/10.1103/PhysRevLett.105.083004)
40. Chapman H.N., Yefanov O.M., Ayer K., White T.A., Barty A., Morgan A., Mariani V., Oberthuer D., Pande K. Continuous diffraction of molecules and disordered molecular crystals. *J. Appl. Crystallogr.* 2017. V. 50. P. 1084–1103. doi: [10.1107/S160057671700749X](https://doi.org/10.1107/S160057671700749X)
41. Hau-Riege S.P., London R.A., Szoke A. Dynamics of biological molecules irradiated by short x-ray pulses. *Phys. Rev. E. Stat. Nonlin. Soft Matter Phys.* 2004. V. 69. Article No. 051906. doi: [10.1103/PhysRevE.69.051906](https://doi.org/10.1103/PhysRevE.69.051906)
42. Lorenz U., Kabachnik N.M., Weckert E., Vartanyants I.A. Impact of ultrafast electronic damage in single particle x-ray imaging experiments. *Phys. Rev. E. Stat. Nonlin. Soft Matter Phys.* 2012. V. 86. Article No. 051911. doi: [10.1103/PhysRevE.86.051911](https://doi.org/10.1103/PhysRevE.86.051911)

43. Ziaja B., Jurek Z., Medvedev N., Saxena V., Son S.-K., Santra R. Towards Realistic Simulations of Macromolecules Irradiated under the Conditions of Coherent Diffraction Imaging with an X-ray Free-Electron Laser. *Photonics*. 2015. V. 2. P. 256–269. doi: [10.3390/photonics2010256](https://doi.org/10.3390/photonics2010256)
44. Kai T., Moribayashi K. Effects of electron-impact ionization on the damage to biomolecules irradiated by XFEL. *Journal of Physics: Conference Series*. 2009. V. 163. Article No. 012035. doi: [10.1088/1742-6596/163/1/012035](https://doi.org/10.1088/1742-6596/163/1/012035)
45. Ziaja B., de Castro Antonio R.B., Weckert E., Moeller T. Modelling dynamics of samples exposed to free-electron-laser radiation with Boltzmann equations. *Eur. Phys. J.* 2006. V. 40. P. 465–480. doi: [10.1140/epjd/e2006-00240-x](https://doi.org/10.1140/epjd/e2006-00240-x)
46. Fortmann-Grote C., Buzmakov A., Jurek Z., Loh N.D., Samoylova L., Santra R., Schneidmiller E.A., Tschentscher T., Yakubov S., Yoon C.H. et al. Start-to-end simulation of single-particle imaging using ultra-short pulses at the European X-ray Free-Electron Laser. *IUCrJ*. 2017. V. 4. P. 560–568. doi: [10.1107/S2052252517009496](https://doi.org/10.1107/S2052252517009496)
47. Coleman C., Bergh M., Scott H.A., Spence J.C., Chapman H.N., Tîmneanu N. Simulations of radiation damage in biomolecular nanocrystals induced by femtosecond X-ray pulses. *J. Mod. Opt.* 2011. V. 58. P. 1486–1497. doi: [10.1080/09500340.2011.597519](https://doi.org/10.1080/09500340.2011.597519)
48. Hau-Riege S.P. Nonequilibrium electron dynamics in materials driven by high-intensity x-ray pulses. *Phys. Rev. E*. 2013. V. 87. P. 053102. doi: [10.1103/PhysRevE.87.053102](https://doi.org/10.1103/PhysRevE.87.053102)
49. Akça B., Erzeneoğlu S. The Mass Attenuation Coefficients, Electronic, Atomic, and Molecular Cross-Sections, Effective Atomic Numbers, and Electron Densities for Compounds of Some Biomedically Important Elements at 59.5 keV. *Science and Technology of Nuclear Installations*. 2014. Article No. 901465. doi: [10.1155/2014/901465](https://doi.org/10.1155/2014/901465)
50. Zeldin O.B., Gerstel M., Garman E.F. RADDOSE-3D: time- and space-resolved modelling of dose in macromolecular crystallography. *J. Appl. Cryst.* 2013. V. 46. P. 1225–1230. doi: [10.1107/S0021889813011461](https://doi.org/10.1107/S0021889813011461)
51. Bury C.S., Brooks-Bartlett C., Walsh S.P., Garman E.F. Estimate your dose: RADDOSE-3D. *Protein Sci.* 2018. V. 27. P. 217–228. doi: [10.1002/pro.3302](https://doi.org/10.1002/pro.3302)
52. Dickerson J.L., McCubbin P.T.N., Garman E.F. RADDOSE-XFEL: femtosecond time-resolved dose estimates for macromolecular X-ray free-electron laser experiments. *J. Appl. Cryst.* 2020. V. 53. P. 549–560. doi: [10.1107/S1600576720000643](https://doi.org/10.1107/S1600576720000643)
53. Owen R.L., Rudino-Pinera E., Garman E.F. Experimental determination of the radiation dose limit for cryocooled protein crystals. *Proc. Natl. Acad. Sci. USA*. 2006. V. 103. P. 4912–4917. doi: [10.1073/pnas.0600973103](https://doi.org/10.1073/pnas.0600973103)
54. de la Mora E., Coquelle N., Bury C.S., Rosenthal M., Holton J.M., Carmichael I., Garman E.F., Burghammer M., Colletier J.P., Weik M. Radiation damage and dose limits in serial synchrotron crystallography at cryo- and room temperatures. *Proc. Natl. Acad. Sci. USA*. 2020. V. 117. P. 4142–4151. doi: [10.1073/pnas.1821522117](https://doi.org/10.1073/pnas.1821522117)
55. Huang B., Bates M., Zhuang, X. Super-resolution fluorescence microscopy. *Annu. Rev. Biochem.* 2009. V. 78. P. 993–1016. doi: [10.1146/annurev.biochem.77.061906.092014](https://doi.org/10.1146/annurev.biochem.77.061906.092014)
56. Rodriguez J.A., Xu R., Chen C.-C., Huang Z., Jiang H., Chen A.L., Raines K.S., Pryor A. Jr, Nam D., Wiegart L. et al. Three-dimensional coherent X-ray diffractive imaging of whole frozen-hydrated cells. *IUCrJ*. 2015. V. 2. P. 575–583. doi: [10.1107/S205225251501235X](https://doi.org/10.1107/S205225251501235X)
57. Howells M.R., Beetz T., Chapman H.N., Cui C., Holton J.M., Jacobsen C.J., Kirz J., Lima E., Marchesini S., Miao H. et al. An assessment of the resolution limitation due to radiation-damage in x-ray diffraction microscopy. *J. Electron Spectrosc. Relat. Phenom.* 2009. V. 170. P. 4–12. doi: [10.1016/j.elspec.2008.10.008](https://doi.org/10.1016/j.elspec.2008.10.008)

58. Kimura T., Joti Y., Shibuya A., Song C., Kim S., Tono K., Yabashi M., Tamakoshi M., Moriya T., Oshima T. et al. Imaging live cell in micro-liquid enclosure by X-ray laser diffraction. *Nat. Commun.* 2014. V. 5. Article No. 3052. doi: [10.1038/ncomms4052](https://doi.org/10.1038/ncomms4052)
59. Borek D., Cymborowski M., Machius M., Minor W., Otwinowski Z. Diffraction data analysis in the presence of radiation damage. *Acta Crystallogr D.* 2010. V. 66. P. 426–436. doi: [10.1107/S0907444909040177](https://doi.org/10.1107/S0907444909040177)
60. Warkentin M.A., Atakisi H., Hopkins J.B., Walko D., Thorn R.E. Lifetimes and spatio-temporal response of protein crystals in intense X-ray microbeams. *IUCrJ.* 2017. V. 4. P. 785–794. doi: [10.1107/S2052252517013495](https://doi.org/10.1107/S2052252517013495)
61. Lomb L., Barends T.R.M., Kassemeyer S., Aquila A., Epp S.W., Erk B., Foucar L., Hartmann R., Rudek B., Rolles D. et al. Radiation damage in protein serial femtosecond crystallography using an x-ray free-electron laser. *Phys. Rev. B. Condens. Matter Mater. Phys.* 2011. V. 84. Article No. 214111. doi: [10.1103/PhysRevB.84.214111](https://doi.org/10.1103/PhysRevB.84.214111)
62. Young L., Kanter E.P., Krässig B., Li Y., March A.M., Pratt S.T., Santra R., Southworth S.H., Rohringer N., Dimauro L.F. et al. Femtosecond electronic response of atoms to ultra-intense X-rays. *Nature.* 2010. V. 466. P. 56–61. doi: [10.1038/nature09177](https://doi.org/10.1038/nature09177)
63. Erk B., Rolles D., Foucar L., Rudek B., Epp S.W., Cryle M., Bostedt C., Schorb S., Bozek J., Rouzee A. et al. Ultrafast charge rearrangement and nuclear dynamics upon inner-shell multiple ionization of small polyatomic molecules. *Phys. Rev. Lett.* 2013. V. 110. Article No. 053003. doi: [10.1103/PhysRevLett.110.053003](https://doi.org/10.1103/PhysRevLett.110.053003)
64. Fukuzawa H., Son S.K., Motomura K., Mondal S., Nagaya K., Wada S., Liu X.J., Feifel R., Tachibana T., Ito Y. et al. Deep inner-shell multiphoton ionization by intense X-ray free-electron laser pulses. *Phys. Rev. Lett.* 2013. V. 110. Article No. 173005. doi: [10.1103/PhysRevLett.110.173005](https://doi.org/10.1103/PhysRevLett.110.173005)
65. Rudenko A., Inhester L., Hanasaki K., Li X., Robatjazi S.J., Erk B., Boll R., Toyota K., Hao Y., Vendrell O. et al. Femtosecond response of polyatomic molecules to ultra-intense hard X-rays. *Nature.* 2017. V. 546. P. 129–132. doi: [10.1038/nature22373](https://doi.org/10.1038/nature22373)
66. Takanashi T., Nakamura K., Kukk E., Motomura K., Fukuzawa H., Nagaya K., Wada S.-I., Kumagai Y., Iablonskyi D., Ito Y. et al. Ultrafast Coulomb explosion of a diiodomethane molecule induced by an X-ray free-electron laser pulse. *Phys. Chem. Chem. Phys.* 2017. V. 19. P. 19707–19721. doi: [10.1039/C7CP01669G](https://doi.org/10.1039/C7CP01669G)
67. Motomura K., Fukuzawa H., Son S.-K., Mondal S., Tachibana T., Ito Y., Kimura M., Nagaya K., Sakai T., Matsunami K. Sequential multiphoton multiple ionization of atomic argon and xenon irradiated by x-ray free-electron laser pulses from SACLA. *J. Phys. B.* 2013. V. 46. Article No. 164024. doi: [10.1088/0953-4075/46/16/164024](https://doi.org/10.1088/0953-4075/46/16/164024)
68. Fukuzawa H., Takanashi T., Kukk E., Motomura K., Wada S.I., Nagaya K., Ito Y., Nishiyama T., Nicolas C., Kumagai Y. et al. Real-time observation of X-ray-induced intramolecular and interatomic electronic decay in CH<sub>2</sub>I<sub>2</sub>. *Nat. Commun.* 2019. V. 10. Article No. 2186. doi: [10.1038/s41467-019-10060-z](https://doi.org/10.1038/s41467-019-10060-z)
69. Wallner M., Eland J.H.D., Squibb R.J., Andersson J., Roos A.H., Singh R., Talae O., Koulentianos D., Piancastelli M.N., Simon M. et al. Coulomb explosion of CD<sub>3</sub>I induced by single photon deep inner-shell ionization. *Sci. Rep.* 2020. V. 1. Article No. 1246.
70. Murphy B.F., Osipov T., Jurek Z., Fang L., Son S.K., Mucke M., Eland J.H., Zhaunerchyk V., Feifel R., Avaldi L. et al. Femtosecond X-ray-induced explosion of C<sub>60</sub> at extreme intensity. *Nat. Commun.* 2014. V. 5. Article No. 4281. doi: [10.1038/ncomms5281](https://doi.org/10.1038/ncomms5281)
71. Berrah N., Sanchez-Gonzalez A., Jurek Z., Obaid R., Xiong H., Squibb R.J., Osipov T., Lutman A., Fang L., Barillot T. et al. Author Correction: Femtosecond-resolved observation of the fragmentation of buckminsterfullerene following X-ray multiphoton ionization. *Nat. Phys.* 2019. V. 15. Article No. 1301. doi: [10.1038/s41567-019-0706-2](https://doi.org/10.1038/s41567-019-0706-2)

72. Nass K., Foucar L., Barends T.R.M., Hartmann E., Botha S., Shoeman R.L., Doak R.B., Alonso-Mori R., Aquila A., Bajt, S. et al. Indications of radiation damage in ferredoxin microcrystals using high-intensity X-FEL beams. *J. Synchrotron Rad.* 2015. V. 22. P. 225–238. doi: [10.1107/S1600577515002349](https://doi.org/10.1107/S1600577515002349)
73. Wang J. Destruction-and-diffraction by X-ray free-electron laser. *Protein Sci.* 2016. V. 25. P. 1585–1592. doi: [10.1002/pro.2959](https://doi.org/10.1002/pro.2959)
74. Inoue I., Inubushi Y., Sato T., Tono K., Katayama T., Kameshima T., Ogawa K., Togashi T., Owada S., Amemiya Y. et al. Observation of femtosecond X-ray interactions with matter using an X-ray-X-ray pump-probe scheme. *Proc. Natl. Acad. Sci. USA.* 2016. V. 113. P. 1492–1497. doi: [10.1073/pnas](https://doi.org/10.1073/pnas)
75. Nass K., Gorel A., Abdullah M.M., Martin A.V., Kloos M., Marinelli A., Aquila A., Barends T.R.M., Decker F.J., Doak B. et al. Structure dynamics in proteins induced by and probed with X-ray free-electron laser pulses. *Nat. Commun.* 2020. V. 11. Article No. 1814. doi: [10.1038/s41467-020-15610-4](https://doi.org/10.1038/s41467-020-15610-4)
76. Opara N.L., Mohacsi I., Makita M., Castano-Diez D., Diaz A., Juranić P., Marsh M., Meents A., Milne C.J., Mozzanica A. et al. Demonstration of femtosecond X-ray pump X-ray probe diffraction on protein crystals. *Struct. Dyn.* 2018. V. 5. Article No. 054303. doi: [10.1063/1.5050618](https://doi.org/10.1063/1.5050618)
77. Munke A., Andreasson J., Aquila A., Awel S., Ayyer K., Barty A., Bean R.J., Berntsen P., Bielecki J., Boutet S. et al. Coherent diffraction of single Rice Dwarf virus particles using hard X-rays at the Linac Coherent Light Source. *Sci. Data.* 2016. V. 3. Article No. 160064. doi: [10.1038/sdata.2016.64](https://doi.org/10.1038/sdata.2016.64)
78. Kurta R.P., Donatelli J.J., Yoon C.H., Berntsen P., Bielecki J., Daurer B.J., DeMirci H., Fromme P., Hantke M.F., Maia F.R.N.C. et al. Correlations in Scattered X-Ray Laser Pulses Reveal Nanoscale Structural Features of Viruses. *Phys. Rev. Lett.* 2017. V. 119. Article No. 158102. doi: [10.1103/PhysRevLett.119.158102](https://doi.org/10.1103/PhysRevLett.119.158102)
79. Östlin C., Tîmneanu N., Jönsson H.O., Ekeberg T., Martin A.V., Caleman C. Reproducibility of single protein explosions induced by X-ray lasers. *Phys. Chem. Chem. Phys.* 2018. V. 20. P. 12381–12389. doi: [10.1039/c7cp07267h](https://doi.org/10.1039/c7cp07267h)
80. Östlin C., Timneanu N., Caleman C., Martin A.V. Is radiation damage the limiting factor in high-resolution single particle imaging with X-ray free-electron lasers? *Struct. Dyn.* 2019. V. 6. Article No. 044103. doi: [10.1063/1.509830](https://doi.org/10.1063/1.509830)
81. Nass K. Radiation damage in protein crystallography at X-ray free-electron lasers. *Acta Crystallogr. D. Struct. Biol.* 2019. V. 75. P. 211–218. doi: [10.1107/S2059798319000317](https://doi.org/10.1107/S2059798319000317)
82. Campbell J.L., Papp T. Widths of the atomic K-N7 levels. *At. Data Nucl. Data Tables.* 2001. V. 77. P. 1–56. doi: [10.1006/adnd.2000.0848](https://doi.org/10.1006/adnd.2000.0848)
83. Son S.-K., Young L., Santra R. Impact of hollow-atom formation on coherent x-ray scattering at high intensity. *Phys. Rev. A.* 2011. V. 83. Article No. 033402. doi: [10.1103/PhysRevA.83.033402](https://doi.org/10.1103/PhysRevA.83.033402)
84. Lunin V.Y., Grum-Grzhimailo A.N., Gryzlova E.V., Sinitsyn D.O., Petrova T.E., Lunina N.L., Balabaev N.K., Tereshkina K.B., Stepanov A.S., Krupyanskii Y.F. Efficient calculation of diffracted intensities in the case of non-stationary scattering by biological macromolecules under XFEL pulse. *Acta Crystallographica D.* 2015. V. 71. P. 293–303. doi: [10.1107/S1399004714025450](https://doi.org/10.1107/S1399004714025450)
85. Chapman H.N., Barty A., Bogan M., Boutet S., Frank M., Hau-Riege S.P., Marchesini S. et al. Femtosecond diffractive imaging with a soft-X-ray free-electron laser. *Nat. Phys.* 2006. V. 2. P. 839–843. doi: [10.1038/nphys461](https://doi.org/10.1038/nphys461)
86. Seibert M.M., Ekeberg T., Maia F.R., Svenda M., Andreasson J., Jönsson O., Odić D., Iwan B., Rocker A., Westphal D. et al. Single mimivirus particles intercepted and imaged with an X-ray laser. *Nature.* 2011. V. 470 P. 78–81. doi: [10.1038/nature09748](https://doi.org/10.1038/nature09748)

87. Hantke M.F., Hasse D., Maia F.R.N.C., Ekeberg T., John K., Svenda M., Loh N.D., Martin A.V., Timneanu N., Larsson D.S.D. et al. High-throughput imaging of heterogeneous cell organelles with an x-ray laser. *Nat. Photonics*. 2014. V. 8. P. 943–949. doi: [10.1038/nphoton.2014.27](https://doi.org/10.1038/nphoton.2014.27)
88. van der Schot G., Svenda M., Maia F.R.N.C., Hantke M., DePonte D.P., Seibert M.M., Aquila A., Schulz J., Kirian R., Liang M., Stellato F. et al. Imaging single cells in a beam of live cyanobacteria with an x-ray laser. *Nat. Commun.* 2015 V. 6. Article No. 5704. doi: [10.1038/ncomms6704](https://doi.org/10.1038/ncomms6704)
89. Ekeberg T., Svenda M., Abergel C., Maia F.R.N.C., Seltzer V., Claverie J.M., Hantke M., Jönsson O., Nettelblad C., van der Schot G. et al. Three-Dimensional Reconstruction of the Giant Mimivirus Particle with an X-Ray Free-Electron Laser. *Phys. Rev. Lett.* 2015. V. 114. Article No. 098102. doi: [10.1103/PhysRevLett.114.098102](https://doi.org/10.1103/PhysRevLett.114.098102)
90. Reddy H.K.N., Yoon C.H., Aquila A., Awel S., Ayyer K., Barty A., Berntsen P., Bielecki J., Bobkov S., Bucher M. Coherent soft X-ray diffraction imaging of coliphage PR772 at the Linac coherent light source. *Sci. Data*. 2017. V.4. Article No. 170079. doi: [10.1038/sdata.2017.79](https://doi.org/10.1038/sdata.2017.79)
91. Daurer B.J., Okamoto K., Bielecki J., Maia F.R.N.C., Muhlig K., Seibert M.M., Hantke M.F., Nettelblad C., Benner W.H., Svenda M. et al. Experimental strategies for imaging bioparticles with femtosecond hard X-ray pulses. *IUCrJ*. 2017. V. 4. P. 251–262. doi: [10.1107/S2052252517003591](https://doi.org/10.1107/S2052252517003591)
92. Lundholm I.V., Sellberg J.A., Ekeberg T., Hantke M.F., Okamoto K., van der Schot G., Andreasson J., Barty A., Bielecki J., Bruza P. et al. Considerations for three-dimensional image reconstruction from experimental data in coherent diffractive imaging. *IUCrJ*. 2018. V. 5. P. 531–541. doi: [10.1107/S2052252518010047](https://doi.org/10.1107/S2052252518010047)
93. DePonte D.P., Weierstall U., Schmidt K., Warner J., Starodub D., Spence J.C.H., Doak R.B. Gas dynamic virtual nozzle for generation of microscopic droplet streams. *J. Phys. D Appl. Phys.* 2008. V. 41. Article No. 195505. doi: [10.1088/0022-3727/41/19/195505](https://doi.org/10.1088/0022-3727/41/19/195505)
94. Yamashita M., Fenn J.B. Electrospray ion source. Another variation on the free-jet theme. *J. Phys. Chem.* 1984. V. 88. P. 4451–4459. doi: [10.1021/j150664a002](https://doi.org/10.1021/j150664a002)
95. Gañán-Calvo A.M., Montanero J.M. Revision of capillary cone-jet physics: Electrospray and flow focusing. *Phys. Rev. E*. 2009. V. 79. Article No. 066305. doi: [10.1103/PhysRevE.79.066305](https://doi.org/10.1103/PhysRevE.79.066305)
96. Hantke M.F., Bielecki J., Kulyk O., Westphal D., Larsson D.S.D., Svenda M., Reddy H.K.N., Kirian R.A., Andreasson J., Hajdu J. et al. Rayleigh-scattering microscopy for tracking and sizing nanoparticles in focused aerosol beams. *IUCrJ*. 2018. V. 5. P. 673–680. doi: [10.1107/S2052252518010837](https://doi.org/10.1107/S2052252518010837)
97. Bielecki J., Hantke M.F., Daurer B.J., Reddy H.K.N., Hasse D., Larsson D.S.D., Gunn L.H., Svenda M., Munke A., Sellberg J.A. et al. Electrospray sample injection for single-particle imaging with x-ray lasers. *Sci. Adv.* 2019. V. 5. Article No. eaav8801. doi: [10.1126/sciadv.aav8801](https://doi.org/10.1126/sciadv.aav8801)
98. Miao J., Hodgson K.O., Ishikawa T., Larabell C.A., LeGros M.A., Nishino Y. Imaging whole *Escherichia coli* bacteria by using single-particle x-ray diffraction. *Proc. Natl. Acad. Sci. USA*. 2003. V. 100. P. 110–112. doi: [10.1073/pnas.232691299](https://doi.org/10.1073/pnas.232691299)
99. Shapiro D., Thibault P., Beetz T., Elser V., Howells M., Jacobsen C., Kirz J., Lima E., Miao H., Neiman A.M. et al. Biological imaging by soft x-ray diffraction microscopy. *Proc. Natl. Acad. Sci. USA*. 2005. V. 102. P. 15343–15346. doi: [10.1073/pnas.0503305102](https://doi.org/10.1073/pnas.0503305102)
100. Song C., Tono K., Park J., Ebisu T., Kim S., Shimada H., Kim S., Gallagher-Jones M., Nam D., Sato T. et al. Multiple application X-ray imaging chamber for single-shot

- diffraction experiments with femtosecond X-ray laser pulses. *J. Appl. Cryst.* 2014. V. 47. P. 188–197. doi: [10.1107/S1600576713029944](https://doi.org/10.1107/S1600576713029944)
101. Robinson I., Schwenke J., Yusuf M., Estandarte A., Zhang F., Chen B., Clark J., Song Ch., Nam D., Joti Y. et al. Towards single particle imaging of human chromosomes at SACLA. *J. Phys. B: At. Mol. Opt. Phys.* 2015. V. 48. Article No. 244007. doi: [10.1088/0953-4075/48/24/244007](https://doi.org/10.1088/0953-4075/48/24/244007)
  102. Seuring C., Ayyer K., Filippaki E., Barthelmess M., Longchamp J.N., Ringler P., Pardini T., Wojtas D.H., Coleman M.A., Dörner K. et al. Femtosecond X-ray coherent diffraction of aligned amyloid fibrils on low background graphene. *Nat. Commun.* 2018. V. 9. Article No. 1836. doi: [10.1038/s41467-018-04116-9](https://doi.org/10.1038/s41467-018-04116-9)
  103. Takayama Y., Yonekura K. Cryogenic coherent X-ray diffraction imaging of biological samples at SACLA: a correlative approach with cryo-electron and light microscopy. *Acta Crystallogr. A.* 2016. V. 72. P. 179–189. doi: [10.1107/S2053273315023980](https://doi.org/10.1107/S2053273315023980)
  104. Altarelli M. The European X-ray free-electron laser facility in Hamburg. *Nucl. Instrum. Methods Phys. Res. B.* 2011. V. 269. P. 2845–2849. doi: [10.1016/j.nimb.2011.04.034](https://doi.org/10.1016/j.nimb.2011.04.034)
  105. von Ardenne B., Mechelke M., Grubmüller H. Structure determination from single molecule X-ray scattering with three photons per image. *Nat. Commun.* 2018. V. 9. Article No. 2375. doi: [10.1038/s41467-018-04830-4](https://doi.org/10.1038/s41467-018-04830-4)
  106. Allahgholi A., Becker J., Bianco L., Bradford R., Delfs A., Dinapoli R., Goettlicher P., Gronewald M., Graafsma H., Greiffenberg D. et al. The adaptive gain integrating pixel detector. *J. Instrum.* 2016. V. 11. Article No. C02066. doi: [10.1088/1748-0221/11/02/C02066](https://doi.org/10.1088/1748-0221/11/02/C02066)
  107. Mezza D., Allahgholi A., Arino-Estrada G., Bianco L., Delfs A., Dinapoli R., Goettlicher P., Graafsma H., Greiffenberg D., Hirsemann H. et al. Characterization of AGIPD1.0: the full scale chip. *Nucl. Instrum. Methods Phys. Res. A.* 2016. V. 838. P. 39–46. doi: [10.1016/j.nima.2016.09.007](https://doi.org/10.1016/j.nima.2016.09.007)
  108. Allahgholi A., Becker J., Delfs A., Dinapoli R., Goettlicher P., Greiffenberg D., Henrich B., Hirsemann H., Kuhn M., Klanner R. et al. The Adaptive Gain Integrating Pixel Detector at the European XFEL. *J. Synchrotron Radiat.* 2019. V. 26. P. 74–82. doi: [10.1107/S1600577518016077](https://doi.org/10.1107/S1600577518016077)
  109. Philipp H.T., Hromalik M., Tate M., Koerner L., Gruner S.M. Pixel array detector for X-ray free electron laser experiments. *Nucl. Instrum. Methods Phys. Res. A.* 2011. V. 649. P. 67–69. doi: [10.1016/j.nima.2010.11.189](https://doi.org/10.1016/j.nima.2010.11.189)
  110. Blaj G., Caragiulo P., Carini G., Dragone A., Haller G., Hart P., Hasi J., Herbst R., Kenney C., Markovic B. et al. Future of ePix detectors for high repetition rate FELs. *AIP Conference Proceedings.* 2016. V. 1741. Article No. 040012. doi: [10.1063/1.495288](https://doi.org/10.1063/1.495288)
  111. Leonarski F., Redford S., Mozzanica A., Lopez-Cuenca C., Panepucci E., Nass K., Ozerov D., Vera L., Olieric V., Buntschu D. et al. Fast and accurate data collection for macromolecular crystallography using the JUNGFR AU detector. *Nat. Methods.* 2018. V. 15. P. 799–804. doi: [10.1038/s41592-018-0143-7](https://doi.org/10.1038/s41592-018-0143-7)
  112. Redford S., Bergamaschi A., Brückner M., Cartier S., Dinapoli R., Ekinci Y., Fröjdh E., Greiffenberg D., Mayilyan D., Mezza D. et al. Calibration status and plans for the charge integrating JUNGFR AU pixel detector for SwissFEL. *J. Instrum.* 2016. V. 11. Article No. C11013.
  113. Goettlicher P., Allahgholi A., Becker J., Bianco L., Delfs A., Dinapoli R., Fretwurst E., Fretwurst E., Graafsma H., Greiffenberg D. et al. AGIPD, the electronics for a high speed X-ray imager at the Eu-XFEL. In: *Proceedings of TIP2014 – Technology and Instrumentation in Particle Physic.* 2014. P. 253.
  114. Mancuso A.P., Aquila A., Batchelor L., Bean R.J., Bielecki J., Borchers G., Doerner K., Giewekemeyer K., Graceffa R., Kelsey O.D. et al. The Single Particles, Clusters and Biomolecules and Serial Femtosecond Crystallography instrument of the European

- XFEL: initial installation. *J. Synchrotron Radiat.* 2019. V. 26. P. 660–676. doi: [10.1107/S1600577519003308](https://doi.org/10.1107/S1600577519003308)
115. Gasthuber M., Dietrich S., Malka J., Kuhn M., Ensslin U., Wrona K., Szuba J. Online & Offline data storage and data processing at the European XFEL facility. *J. Phys.: Conf. Ser.* 2017. V. 898. Article No. 062049. doi: [10.1088/1742-6596/898/6/062049](https://doi.org/10.1088/1742-6596/898/6/062049)
  116. Hauf S., Heisen B., Aplin S., Beg M., Bergemann M., Bondar V., Boukhelef D., Danilevsky C., Ehsan W., Essenov S. et al. The Karabo distributed control system. *J. Synchrotron Radiat.* 2019. V. 26. P. 1448–1461. doi: [10.1107/S1600577519006696](https://doi.org/10.1107/S1600577519006696)
  117. Fangohr H., Beg M., Bondar V., Boukhelef D., Brockhauser S., Danilevski C., Ehsan W., Essenov S.G., Flucke G., Giovanetti G. et al. Data Analysis Support in Karabo at European XFEL. In: *Proc. 16th Int. Conf. on Accelerator and Large Experimental Control Systems (ICALEPCS'17) (Barcelona, Spain, Oct. 2017)*. 2018. P. 245–252. doi: [10.18429/JACoW-ICALEPCS2017-TUCPA01](https://doi.org/10.18429/JACoW-ICALEPCS2017-TUCPA01)
  118. Rose M., Bobkov S., Ayyer K., Kurta R.P., Dzhigaev D., Kim Y.Y., Morgan A.J., Yoon C.H., Westphal D., Bielecki J. et al. Single-particle imaging without symmetry constraints at an X-ray free-electron laser. *IUCrJ.* 2018. V. 5. P. 727–736. doi: [10.1107/S205225251801120X](https://doi.org/10.1107/S205225251801120X)
  119. Daurer B.J., Hantke M.F., Nettelblad C, Maia F.R.N.C. Hummingbird: monitoring and analyzing flash X-ray imaging experiments in real time. *J. Appl. Cryst.* 2016. V. 49. P. 1042–1047. doi: [10.1107/S1600576716005926](https://doi.org/10.1107/S1600576716005926)
  120. Barty A., Kirian R.A., Maia F.R.N.C., Hantke M., Yoon C.H., White T.A., Chapman H. Cheetah: software for high-throughput reduction and analysis of serial femtosecond X-ray diffraction data. *J. Appl. Cryst.* 2014. V. 47. P. 1118–1131. doi: [10.1107/S1600576714007626](https://doi.org/10.1107/S1600576714007626)
  121. Foucar L., Barty A., Coppola N., Hartmann R., Holl P., Hoppe U., Kassemeyer S., Kimmel N., Küpper J., Scholz et al. CASS–CFEL–ASG software suite. *Comput. Phys. Commun.* 2012. V. 183. P. 2207–2213. doi: [10.1016/j.cpc.2012.04.023](https://doi.org/10.1016/j.cpc.2012.04.023)
  122. Foucar L. CFEL-ASG Software Suite (CASS): usage for free-electron laser experiments with biological focus. *J. Appl. Crystallogr.* 2016. V. 49. P. 1336–1346. doi: [10.1107/S1600576716009201](https://doi.org/10.1107/S1600576716009201)
  123. Damiani D., Dubrovin M., Gaponenko I., Kroeger W., Lane T.J., Mitra A., O'Grady C.P., Salnikov A., Sanchez-Gonzalez A., Schneider D., Yoon C.H. Linac Coherent Light Source data analysis using psana. *J. Appl. Cryst.* 2016. V. 49. P. 672–679. doi: [10.1107/S1600576716004349](https://doi.org/10.1107/S1600576716004349)
  124. Coifman R.R., Lafon S. Diffusion maps. *Appl. Comput. Harmon. Anal.* 2006. V. 21. P. 5–30. doi: [10.1016/j.acha.2006.04.006](https://doi.org/10.1016/j.acha.2006.04.006)
  125. Giannakis D., Schwander P., Ourmazd A. The symmetries of image formation by scattering. I. Theoretical framework. *Opt. Express.* 2012. V. 20. P. 12799–12826. doi: [10.1364/OE.20.012799](https://doi.org/10.1364/OE.20.012799)
  126. Yoon C.H., Schwander P., Abergel C., Andersson I., Andreasson J., Aquila A., Bajt S., Barthelmeß M., Barty A., Bogan M.J., Bostedt C., Bozek J. et al. Unsupervised classification of single-particle X-ray diffraction snapshots by spectral clustering. *Opt. Express.* 2011. V. 19. P. 16542–16549. doi: [10.1364/OE.19.016542](https://doi.org/10.1364/OE.19.016542)
  127. Giewekemeyer K., Aquila A., Loh N.D., Chushkin Y., Shanks K.S., Weiss J.T., Tate M.W., Philipp H.T., Stern S., Vagovic P. et al. Experimental 3D coherent diffractive imaging from photon-sparse random projections. *IUCrJ.* 2019. V. 20. P. 357–365. doi: [10.1107/S2052252519002781](https://doi.org/10.1107/S2052252519002781)
  128. Ayyer K., Morgan A.J., Aquila A., DeMirci H., Hogue B.G., Kirian R.A., Xavier P.L., Yoon C.H., Chapman H.N., Barty A. Low-signal limit of X-ray single particle diffractive imaging. *Opt. Express.* 2019. V. 27. P. 37816–37833. doi: [10.1364/OE.27.037816](https://doi.org/10.1364/OE.27.037816)

129. Loh N.D., Elser V. Reconstruction algorithm for single-particle diffraction imaging experiments. *Phys. Rev. E*. 2009. V. 80. Article No. 026705. doi: [10.1103/PhysRevE.80.026705](https://doi.org/10.1103/PhysRevE.80.026705)
130. Ayyer K., Lan Ti-Yen, Elser V., Loh N.D. Dragonfly: an implementation of the expand–maximize–compress algorithm for single-particle imaging. *J. Appl. Crystallogr.* 2016. V. 49. P. 1320–1335. doi: [10.1107/S1600576716008165](https://doi.org/10.1107/S1600576716008165)
131. Yoon C.H., Yurkov M.V., Schneidmiller E.A., Samoylova L., Buzmakov A., Jurek Z., Ziaja B., Santra R., Loh N.D., Tschentscher T. et al. A comprehensive simulation framework for imaging single particles and biomolecules at the European X-ray Free-Electron Laser. *Sci. Rep.* 2016. V. 6. Article No. 24791. doi: [10.1038/srep24791](https://doi.org/10.1038/srep24791)
132. Hantke M.F., Ekeberg T., Maia F.R.H.C. A simulation tool for flash X-ray imaging. *J. Appl. Cryst.* 2016. V. 49. P. 1356–1362. doi: [10.1107/S1600576716009213](https://doi.org/10.1107/S1600576716009213)
133. Lunin V.Y., Lunina N.L., Petrova T.E. Mask-Based Approach in Phasing and Restoring of Single-Particle Diffraction Data. *Mathematical Biology and Bioinformatics*. 2020. V. 15. № S. P. t1–t20. doi: [10.17537/2020.15.t1](https://doi.org/10.17537/2020.15.t1)
134. Bricogne G. Geometric sources of redundancy in intensity data and their use for phase determination. *Acta Crystallographica A*. 1974. V. 30. P. 395–405. doi: [10.1107/S0567739474010722](https://doi.org/10.1107/S0567739474010722)
135. Bricogne G. Methods and programs for direct-space exploitation of geometric redundancies. *Acta Crystallographica A*. 1976. V. 32. P. 832–847. doi: [10.1107/S0567739476001691](https://doi.org/10.1107/S0567739476001691)
136. Lunin V.Y. Use of the fast differentiation algorithm for phase refinement in protein crystallography. *Acta Crystallographica A*. 1985. V. 41. P. 551–556. doi: [10.1107/S0108767385001209](https://doi.org/10.1107/S0108767385001209)
137. Podjarny A.D., Rees B., Urzhumtsev A.G. Density modification in X-ray crystallography. In: *Methods in Molecular Biology, Crystallographic Methods and Protocols*. Eds. Jones C., Milloy B, Sanderson M.R. Totowa, New Jersey: Humana Press, 1996. P. 205–226. (Methods in Molecular Biology, Vol. 56). doi: [10.1385/0-89603-259-0:205](https://doi.org/10.1385/0-89603-259-0:205)
138. Zhang K.Y.J., Cowtan K.D., Main P. Phase improvement by iterative density modification. In: *International Tables for Crystallography. Vol. F*. Eds. Arnold E., Himmel D.M., Rossmann M.G. Chichester: John Wiley and Sons, 2012. P. 385–400. doi: [10.1107/97809553602060000847](https://doi.org/10.1107/97809553602060000847)
139. Fienup J.R. Reconstruction of an object from the modulus of its Fourier transform. *Optics Letters*. 1978. V. 3. N. 1. P. 27–29. doi: [10.1364/OL.3.000027](https://doi.org/10.1364/OL.3.000027)
140. Wang B.C. Resolution of phase ambiguity in macromolecular crystallography. *Methods in Enzymology*. 1985. V. 115. P. 90–111. doi: [10.1016/0076-6879\(85\)15009-3](https://doi.org/10.1016/0076-6879(85)15009-3)
141. Abrahams J.P. Bias reduction in phase refinement by modified interference functions: introducing the  $\gamma$ -correction. *Acta Crystallographica D*. 1997. V. 53. P. 371–376. doi: [10.1107/S0907444996015272](https://doi.org/10.1107/S0907444996015272)
142. Oslányi G., Sütő A. Ab initio structure solution by charge flipping. *Acta Crystallographica A*. 2004. V. 60. P. 134–141. doi: [10.1107/S0108767303027569](https://doi.org/10.1107/S0108767303027569)
143. Marchesini S. A unified evaluation of iterative projection algorithms for phase retrieval. *Rev. Sci. Instrum.* 2007. V. 78. Article No. 011301. doi: [10.1063/1.2403783](https://doi.org/10.1063/1.2403783)
144. Maia F.R.N.C., Ekeberg T., Spoel D., Hajdu J. Hawk: the image reconstruction package for coherent X-ray diffractive imaging. *J. Applied Crystallography*. 2010. V. 43. P. 1535–1539. doi: [10.1107/S0021889810036083](https://doi.org/10.1107/S0021889810036083)
145. Millane R., Lo V.L. Iterative projection algorithms in protein crystallography. I. Theory. *Acta Crystallographica A*. 2013. V. 69. P. 517–527. doi: [10.1107/S0108767313015249](https://doi.org/10.1107/S0108767313015249)
146. Urzhumtsev A.G. *The use of local averaging in analysis of macromolecule images at electron density distribution maps*: Preprint. Pushchino, 1985 (in Russ.).

147. Urzhumtsev A.G., Lunin V.Y., Luzyanina T.B. Bounding a Molecule in a Noisy Synthesis. *Acta Crystallographica A*. 1989. V. 45. P. 34–39. doi: [10.1107/s0108767388008955](https://doi.org/10.1107/s0108767388008955)
148. Marchesini S., He H., Chapman H.N., Hau-Riege S.P., Noy A., Howells M.R., Weierstall U., Spence J.H.C. X-ray image reconstruction from a diffraction pattern alone. *Phys. Rev. B*. 2003. V. 68. Article No. 140101(R). doi: [10.1103/PhysRevB.68.140101](https://doi.org/10.1103/PhysRevB.68.140101)
149. Lunin V.Y., Lunina N.L., Petrova T.E. The use of connected masks for reconstructing the single particle image from X-ray diffraction data. *Mathematical Biology and Bioinformatics*. 2015. V. 10. № S. P. t1–t19. doi: [10.17537/2015.10.t1](https://doi.org/10.17537/2015.10.t1)
150. Lunin V.Y., Lunina N.L., Petrova T.E., Baumstark M.W., Urzhumtsev A.G. Mask-based approach to phasing of single-particle diffraction data. *Acta Crystallographica D*. 2016. V. 72. P. 147–157. doi: [10.1107/S2059798315022652](https://doi.org/10.1107/S2059798315022652)
151. Lunin V.Y., Lunina N.L., Petrova T.E., Baumstark M.W., Urzhumtsev A.G. Mask-based approach to phasing of single-particle diffraction data. II. Likelihood-based selection criteria. *Acta Crystallographica D*. 2019. V. 75. P. 79–89. doi: [10.1107/S2059798318016959](https://doi.org/10.1107/S2059798318016959)
152. Lunina N.L., Petrova T.E., Urzhumtsev A.G., Lunin V.Y. The use of connected masks for reconstructing the single particle image from X-ray diffraction data. II. The dependence of the accuracy of the solution on the sampling step of experimental data. *Mathematical Biology and Bioinformatics*. 2015. V. 10. № S. P. t56–t72. doi: [10.17537/2015.10.t56](https://doi.org/10.17537/2015.10.t56)
153. Lunina N.L., Petrova T.E., Urzhumtsev A.G., Lunin V.Y. The Use of Connected Masks for Reconstructing the Single Particle Image from X-Ray Diffraction Data. III. Maximum-Likelihood Based Strategies to Select Solution of the Phase Problem. *Mathematical Biology and Bioinformatics*. 2018. V. 13. № S. P. t70–t83. doi: [10.17537/2018.13.t70](https://doi.org/10.17537/2018.13.t70)
154. Mancuso A.P., Gorniak Th., Staier F., Yefanov O.M., Barth R., Christophis C., Reime B., Gulden J., Singer A., Pettit M.E. et al. Coherent imaging of biological samples with femtosecond pulses at the free electron laser FLASH. *New J. Phys.* 2010. V. 12. Article No. 035003. doi: [10.1088/1367-2630/12/3/035003](https://doi.org/10.1088/1367-2630/12/3/035003)
155. Seibert M.M., Boutet S., Svenda M., Ekeberg T., Maia F.R.N.C., Bogan M.J., Nicusor Timneanu N., Anton Barty A., Stefan Hau-Riege S., Caleman C. Femtosecond diffractive imaging of biological cells. *J. Phys. B: At. Mol. Opt. Phys.* 2010. V. 43. Article No. 194015. doi: [10.1088/0953-4075/43/19/194015](https://doi.org/10.1088/0953-4075/43/19/194015)
156. Gallagher-Jones M., Bessho Y., Kim S., Park J., Kim S., Nam D., Kim C., Kim Y., Noh do Y., Miyashita O. et al. Macromolecular structures probed by combining single-shot free-electron laser diffraction with synchrotron coherent X-ray imaging. *Nat. Commun.* 2014. V. 5. Article No. 3798. doi: [10.1038/ncomms4798](https://doi.org/10.1038/ncomms4798)
157. Xu R., Jiang H., Song C., Rodriguez J.A., Huang Z., Chen C.-C., Nam D., Park J., Gallagher-Jones M., Kim S. et al. Single-shot three-dimensional structure determination of nanocrystals with femtosecond X-ray free-electron laser pulses. *Nat. Commun.* 2014. V. 5. Article No. 4061. doi: [10.1038/ncomms5061](https://doi.org/10.1038/ncomms5061)
158. Takayama Y., Inui Y., Sekiguchi Y., Kobayashi A., Oroguchi T., Yamamoto M., Matsunaga S., Nakasako M. Coherent X-Ray Diffraction Imaging of Chloroplasts from Cyanidioschyzon merolae by Using X-Ray Free Electron Laser. *Plant Cell Physiol.* 2015. V. 56. P. 1272–1286. doi: [10.1093/pcp/pcv032](https://doi.org/10.1093/pcp/pcv032)
159. Nakano M., Osamu Miyashita O., Jonic S., Tokuhisa A., Tama F. Single-particle XFEL 3D reconstruction of ribosome-size particles based on Fourier slice matching: requirements to reach subnanometer resolution. *J. Synchrotron Radiat.* 2018. V. 25. P. 1010–1021. doi: [10.1107/S1600577518005568](https://doi.org/10.1107/S1600577518005568)

160. Maia F.R.N.C. The Coherent X-ray Imaging Data Bank. *Nat. methods*. 2012. V. 9. P. 854–855. doi: [10.1038/nmeth.2110](https://doi.org/10.1038/nmeth.2110)
161. Fan J., Sun Z., Wang Y., Park J., Kim S., Gallagher-Jones M., Kim Y., Song C., Yao S., Zhang J. et al. Single-pulse enhanced coherent diffraction imaging of bacteria with an X-ray free-electron laser. *Sci. Rep.* 2016. V. 6. Article No. 34008. doi: [10.1038/srep34008](https://doi.org/10.1038/srep34008)
162. Hosseinizadeh A., Mashayekhi G., Copperman J., Schwander P., Dashti A., Sepehr R., Fung R., Schmidt M., Yoon C.H., Hogue B.G. et al. Conformational landscape of a virus by single-particle X-ray scattering. *Nat. Methods*. 2017. V. 4. P. 877–881. doi: [10.1038/nmeth.4395](https://doi.org/10.1038/nmeth.4395)
163. Aquila A., Barty A., Bostedt C., Boutet S., Carini G., dePonte D., Drell P., Doniach S., Downing K.H., Earnest T. The linac coherent light source single particle imaging road map. *Structural Dynamics*. 2015. V. 2. Article No. 041701. doi: [10.1063/1.4918726](https://doi.org/10.1063/1.4918726)

Received 23.12.2020.

Published 31.12.2020.